Accepted Manuscript

Title: The effects of filamentar Ni, graphene and lithium amide ($LiNH_2$) additives on the dehydrogenation behavior of mechano-chemically synthesized crystalline manganese borohydride ($Mn(BH_4)_2$) and its solvent filtration/ xtraction

Authors: Robert A. Varin, Amirreza Shirani Bidabadi, Marek Polanski, Mazda Biglari, Leszek Stobinski

PII: S0025-5408(17)32785-X
DOI: https://doi.org/10.1016/j.materresbull.2017.12.051
Reference: MRB 9768

To appear in: *MRB*

Received date: 17-7-2017
Revised date: 10-12-2017
Accepted date: 31-12-2017

Please cite this article as: Varin RA, Bidabadi AS, Polanski M, Biglari M, Stobinski L, The effects of filamentar Ni, graphene and lithium amide ($LiNH_2$) additives on the dehydrogenation behavior of mechano-chemically synthesized crystalline manganese borohydride ($Mn(BH_4)_2$) and its solvent filtration/ xtraction, *Materials Research Bulletin* (2010), https://doi.org/10.1016/j.materresbull.2017.12.051

The effects of filamentary Ni, graphene and lithium amide ($LiNH_2$) additives on the dehydrogenation behavior of mechano-chemically synthesized crystalline manganese borohydride ($Mn(BH_4)_2$) and its solvent filtration/extraction

Robert A. Varin[1*], Amirreza Shirani Bidabadi[1], Marek Polanski[2], Mazda Biglari[3], Leszek Stobinski[4]

[1]*Department of Mechanical and Mechatronics Engineering and Waterloo Institute for Nanotechnology, University of Waterloo, 200 University Ave. W., Waterloo, Ontario, Canada N2L 3G1*

[2]*Faculty of Advanced Technology and Chemistry, Military University of Technology, 2 Kaliskiego Str., 00-908 Warsaw, Poland*

[3]*Department of Chemical Engineering, University of Waterloo, 200 University Ave. W., Waterloo, Ontario, Canada N2L 3G1*

[4]*Faculty of Chemical and Process Engineering, Graphene Laboratory, Warsaw University of Technology, Warynskiego 1, 00-645 Warsaw, Poland*

---

[*]Corresponding author: E-mail address: *robert.varin@uwaterloo.ca*

Graphical abstract

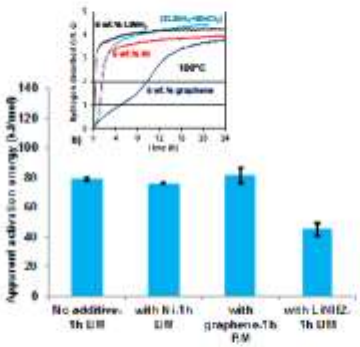

(a) Apparent activation energy (kJ/mol) for dehydrogenation for the samples with and without additives after 1h ball milling and (b) comparison of isothermal dehydrogenation curves at 100°C for the samples with and without additives.

(a) Apparent activation energy (kJ/mol) for dehydrogenation for the samples with and without additives after 1h ball milling and (b) comparison of isothermal dehydrogenation curves at 100°C for the samples with and without additives.

Highlights

- Effect of graphene, filamentary Ni and $LiNH_2$ on the synthesis of $Mn(BH_4)_2$ investigated
- Mechanical dehydrogenation observed for filamentary Ni and $LiNH_2$ but not for graphene
- All additives suppressed the release of B_2H_6 during thermal decomposition of $Mn(BH_4)_2$ with filamentary Ni being the strongest suppressor
- The $LiNH_2$ additive reduced the apparent activation energy for dehydrogenation to 44.9±4.3 kJ/mol
- During the process of solvent filtration and extraction of the ($Mn(BH_4)_2$/LiCl) sample, a dimetallic hydride [{$Li(Et_2O)_2$}$Mn_2(BH_4)_5$] instead of crystalline $Mn(BH_4)_2$ found.

Abstract

Dehydrogenation properties of mechano-chemically synthesized crystalline $Mn(BH_4)_2$ hydride without and with ultrafine filamentary carbonyl nickel (Ni), graphene and $LiNH_2$ were investigated. It is reported for the first time that all additives suppressed the release of B_2H_6 with the filamentary Ni additive being the most effective suppressor of B_2H_6. In DSC, the decomposition peak of $Mn(BH_4)_2$ was endothermic. The estimated apparent activation energy for isothermal dehydrogenation was dramatically reduced to 44.9±4.3 kJ/mol for the 5 wt.% $LiNH_2$ additive from about 76-81 kJ/mol range for the additive-free sample and 5 wt.% filamentary Ni and graphene additives. The most striking finding, that has never been reported in the literature, is that the process of solvent filtration and extraction of the mechano-chemically synthesized ($Mn(BH_4)_2$/LiCl) sample, resulted in the crystallization of a dimetallic borohydride solvate [{$Li(Et_2O)_2$}$Mn_2(BH_4)_5$] instead of crystalline $Mn(BH_4)_2$. Its dehydrogenation behavior was investigated isothermally and by TGA/DSC.

Keywords: Hydride hydrogen storage; Mechano-chemical activation synthesis; Manganese borohydride $Mn(BH_4)_2$; Additives; Solvent filtration/extraction; Dehydrogenation behavior

1. Introduction

Hydrogen (H_2) plays a vital role in the decisive shift from economies dependent on fossil fuels to the ones based on renewable and clean resources. The solid-state metal hydrides are deemed promising as H_2 sources due to their high volumetric hydrogen capacity and the fact that they do not suffer the drawbacks experienced by compressed gaseous and liquid hydrogen, such as large thermal losses and safety problems [1]. Solid hydrides can be used for supplying very clean gaseous H_2 to fuel cell (FC) stacks for automotive sector [1-3]. Unfortunately, solid-state H_2 storage in hydrides has serious constraints for the automotive sector, the most important of which is the inability to meet the need for “on board” rehydrogenation. So far, this and other very serious constraints preclude a full implementation of solid state H_2 storage in the automotive sector [3]. However, some commercial market applications for solid-state hydrogen storage systems may not critically require “on board” rehydrogenation. Such H_2 storage/generation systems can utilize disposable H_2 cartridges of various sizes whose thermal decomposition products could be either regenerated “off board”, after dehydrogenation, or converted into other

useful chemicals. A number of potential, non-automotive applications exist, such as portable electronic devices, stationary auxiliary power systems, off road vehicles, drones, bulk hydrogen storage, air transportation and many others [2, 3].

Lithium borohydride, $LiBH_4$, which is a relatively expensive hydride, exhibits the highest theoretical hydrogen capacity of about 18 wt.% of all solid hydrides. Unfortunately, its decomposition temperature, higher than 400°C, is too high for any practical application. The pertinent hydrides should be capable of desorbing H_2 from a hydride reservoir within the coolant temperature range provided by the waste heat generated by the FC stack, usually not exceeding about 80-100°C, under H_2 pressure slightly above 1 bar [2, 3].

Therefore, since $LiBH_4$ in its pure form is practically useless, it is more convenient to convert it into another hydride that would be able to desorb H_2 at a much lower temperature range than that for $LiBH_4$. An interesting candidate hydride for potential non-automotive hydrogen generation/storage, which can be synthesized from $LiBH_4$, is manganese borohydride ($Mn(BH_4)_2$) exhibiting a still impressive theoretical gravimetric H_2 capacity of 9.5 wt.%. It can be synthesized in solid state by mechano-chemical activation synthesis (MCAS) [4-10] according to the following reaction:

$$nLiBH_4 + MnCl_2 \rightarrow Mn(BH_4)_2 + 2LiCl + (n-2)LiBH_4 \quad (1)$$

The presence of LiCl which is formed as a "dead weight" salt byproduct, reduces the practical capacity of H_2 in the synthesized product. The capacity of hydrogen for n=2 (no retained $LiBH_4$) is 4.76 wt.% H_2, a nearly half of its theoretical H_2 capacity. Therefore, an efficient removal of LiCl from the mixture with $Mn(BH_4)_2$ (Eq. (1) is of great importance. Another problem with $Mn(BH_4)_2$, upon its decomposition, is a release of varying quantities of diborane (B_2H_6), simultaneously with hydrogen [6-11], which reduces the purity of H_2 gas and could be damaging to the membrane of a Proton Exchange Membrane (PEM) fuel cell. Previous studies have not identified any efficient way to efficiently suppress B_2H_6 formation during the decomposition process.

A solvent-mediated synthesis (wet) method has been reported in the literature for the synthesis of various complex hydrides. $Mg(AlH_4)_2$ was obtained based on the metathesis reaction of $NaAlH_4$ and $MgCl_2$ in diethyl ether (Et_2O) and subsequent purification using Soxhlet extraction [12]. Using the same method, $Eu(BH_4)_2$ and $Sm(BH_4)_2$, free from solvent (dimethyl sulfide) and LiCl were also achieved [13]. Pure $Mg(BH_4)_2$ was obtained using the reaction of Et_3NBH_3 and MgH_2

[14]. Richter et al. [15] successfully synthesized $Mn(BH_4)_2$ through reaction of $MnCl_2$ with $LiBH_4$ in a toluene/dimethylsulfide mixture at room temperature which yielded halide and solvent-free manganese borohydride after extraction with dimethylsulfide (DMS) and subsequent removal of residual solvent. Tumanov et al. [16] studied the reaction of $MnCl_2$ with MBH_4 (M = Li^+, Na^+, K^+) in Et_2O. They synthesized new intermediates [{$M(Et_2O)_2$}$Mn_2(BH_4)_5$] (M=Li^+, Na^+) identified by X-ray diffraction. The solvent removal in a vacuum from the [{$Li(Et_2O)_2$}$Mn_2(BH_4)_5$] intermediate hydride led to $Mn(BH_4)_2$ contaminated with LiCl, presumably due to an efficient trapping of the latter salt by the [$Mn(BH_4)_2$–Et_2O] system, while the solvent removal from the [{$Na(Et_2O)_2$}$Mn_2(BH_4)_5$] intermediate produced chlorine-free $Mn(BH_4)_2$ accompanied with $NaBH_4$. Using KBH_4 led to the formation of $K_2Mn(BH_4)_4$ as a second phase.

The attempt to remove the NaCl salt from the product of MCAS from a ($Mg(AlH_4)_2$+2NaCl) mixture and the LiCl from a ($Ca(AlH_4)_2$-2LiCl) mixture, in both cases using Et_2O and THF in a Soxhlet apparatus, was reported by Mamatha et al. [17]. They also reported that complex removal of THF could not be achieved.

Most recently, we reported [18] that NaCl could be effectively removed by diethyl ether (Et_2O) solvent extraction from a mixture with an amorphous $Mn(BH_4)_2$-type hydride which transformed to crystalline $Mn(BH_4)_2$ during a solvent extraction process.

The current work has the following objectives: (1) to study the effects of additives such as ultrafine filamentary nickel Ni, graphene (graphene oxide) and $LiNH_2$ on suppressing the formation of B_2H_6 during decomposition, (2) to study the possible effects of those additives on the mechanical and thermal dehydrogenation of mechano-chemically synthesized $Mn(BH_4)_2$, (3) to employ a simple diethyl ether (Et_2O)-based solvent filtration/extraction method to remove, at least partially, the LiCl salt from a solid mixture with $Mn(BH_4)_2$ (Eq. (1)) and finally, (4) to investigate the dehydrogenation behavior of LiCl-free solvent extracted material.

2. Experimental

In total, four mixtures were synthesized from the as-received powders. The first mixture was composed of the commercial lithium borohydride ($LiBH_4$) (95% purity) and $MnCl_2$ (99.99% purity), both from Alfa Aesar (Canada) in the molar ratio of 2 to 1. The second mixture with the same 2:1 molar ratio of ($LiBH_4$) and $MnCl_2$ was made with the addition of 5 wt.% ultrafine filamentary carbonyl nickel supplied by Cnem Corp (Canada), referred to as “filamentary Ni” in

the text. The third mixture contained the addition of 5 wt.% flake-reduced graphene oxide (FL-rGO), referred to as "graphene", obtained from Nanomaterials (http://www.nanomaterials.pl). The FL-rGO product consists of 2-3 stacked nanostructure graphene layers and contains ~9.6 wt.% % of oxygen and ~1 wt.% H_2 (the exact chemical elemental analysis can be found at http://www.nanomaterials.pl). The graphene product is amorphous and contains 26-30 at. % of oxygen. The fourth mixture contained 5 wt.% $LiNH_2$ that was ordered from Sigma Aldrich with a purity of 95%.

In order to avoid reactions between the powder samples and moisture or oxygen from air, all processes during preparation of the samples were handled in a glove box containing a moisture-absorbing Drierite granulated compound. Before handling, the glove box was purged a few times with high purity argon gas (99.999% purity).

Mechano-chemical activation synthesis (MCAS) of the powder mixtures was carried out for 1h in an ultra-high purity hydrogen gas atmosphere (purity 99.999%) at ~300 kPa pressure in the magneto-ball mill, Uni-Ball-Mill 5, manufactured by A.O.C. Scientific Engineering Pty Ltd, Australia [1, 19-21]. Strong impact mode (IMP68) was used for milling, with two magnets positioned at 6 and 8 o'clock, at the distances from the vial of ~10 and ~2 mm, respectively. The milling media consisted of four 25-mm diameter steel balls, each with a mass of 65 g. The mill rotation speed and the ball-to-powder weight ratio (R) were ~200 rpm and 132, respectively. During milling, the vial was continuously cooled by an air fan. The release of hydrogen during ball milling was monitored and estimated from the pressure increase in the milling vial measured by a pressure gauge, using ideal gas law [1] and expressed in wt.% with respect to the *total* weight of the powder sample. The accuracy was ±0.1 wt.% H_2.

The hydrogen thermal desorption/absorption was evaluated by means of a second-generation volumetric Sieverts-type apparatus custom-built by A.O.C. Scientific Engineering Pty Ltd., Australia [22]. An approximately 30-40 mg sample was used in a desorption test. Before starting this test, the inner tubing of the apparatus was evacuated and purged four times with hydrogen. The furnace of the apparatus was heated separately to the desired test temperature and subsequently inserted onto a tightly sealed powder sample reactor, inside which an atmospheric pressure of 1 bar H_2 was maintained. The powder sample in the reactor took ~400s to reach the furnace temperature of 100-200 °C, which is negligible compared to the desorption completion time. Hence, the test can be considered as "isothermal". Desorption curves were corrected for the

hydrogen gas expansion due to the increase in temperature. The amount of desorbed hydrogen was calculated from the ideal gas law, as described in details in [1], and expressed in wt.% with respect to the *total weight* of the powder sample. The calibrated accuracy of the desorbed hydrogen capacity was about ±0.1 wt.% H_2 and that of temperature reading and stabilization ±0.1 °C.

The apparent activation energy for volumetric hydrogen desorption was estimated using the registered dehydrogenation curves by applying a simple Arrhenius equation [1] following Sandrock et al. [23]

$$k = k_o e^{-E_A / RT} \quad (2)$$

where k is the rate of hydrogen desorption, in the convenient engineering term of wt.%H_2/h measured from the slope of the volumetric hydrogen desorption curves registered by the Sieverts-type apparatus (the selected linear portion of each pertinent dehydrogenation curve was fitted by a linear equation used to obtain its slope) [23, 24], where E_A is the activation energy in kJ/mol, R is the gas constant (8.314472 J/mol K), and T is the absolute temperature (K). The measured rates were plotted in the Arrhenius form as ln k vs. 1000/RT.

The solvent filtration/extraction process was already shown schematically in Fig. 1 in [18]. The ball milled ($2LiBH_4$+$MnCl_2$) powders, with and without additives, were mixed with diethyl ether (Et_2O) with the mass ratio of 1:4 and subsequently stirred for 2h at room temperature (RT) at a rotational speed of 200 rpm, in order to dissolve the newly formed $Mn(BH_4)_2$ in the Et_2O solvent and separate it from the LiCl. The solution after stirring was injected into a 60 ml syringe and filtered with a syringe filter having a 0.2µm hole size. The filtering was done to collect LiCl at the filter and allow dissolved $Mn(BH_4)_2$ to pass through the filter. In order to extract $Mn(BH_4)_2$ from the solution in Et_2O, an evaporation process was carried out on the solution after filtering, at room temperature and also on a hot plate at different temperatures of 32, 42 and 52°C, accompanied by simultaneous vigorous stirring at 1000 rpm to agitate the solution. The dry powder product after evaporation at this stage is refereed to hereafter as 1st EXT, with an additional notation to note the different temperatures used (e.g., 1st EXT at 42 °C). The powders left after the 1st EXT at different temperatures were mixed with diethyl ether again with the same mass ratio (1:4), stirred for the same time duration and, finally filtered for the second time. Similarly, the solution after the 2nd extraction was kept at different temperatures for evaporation.

The dry powder after this process is hereafter referred to as 2nd EXT, with an additional notation for the different temperatures used (e.g., 2nd EXT at 42 °C). The solvent filtration/extraction procedure was also carried out in the glove box which was filled with high-purity argon gas (99.999% purity). It is worth to note that Et_2O was employed as a solvent because LiCl is poorly soluble in Et_2O while $Mn(BH_4)_2$ is efficiently soluble in this solvent [16].

The structural changes of the powder mixtures were characterized by X-ray powder diffraction (XRD) on a Bruker D8 diffractometer using monochromated $CuK\alpha_1$ radiation (λ=0.15406 nm) produced at an accelerating voltage of 40 kV and a current of 30 mA. The scan range was from 2θ=10° to 90° and the rate was 1.2° min^{-1} with a step size of 0.02°. Every time, the same quantity of powder was loaded into a custom-made brass holder with a Cu/glass plate and a Kapton window transmittable for X-rays in the upper part of the sample holder, within a glove box evacuated, Ar purged and subsequently filled with high purity Ar.

The morphology of the as-received Ni, graphene, ball milled powders after MCAS and solvent extraction was investigated by using the LEO 1550 high resolution, field emission scanning electron microscope (FESEM) and employing a secondary electron mode.

The differential scanning calorimetry (DSC) analysis was conducted simultaneously with the thermogravimetric analysis (TGA) on a Setaram Sensys Evo 3d analyzer (France). The analyzer was coupled with a quadrupole mass spectrometer Hiden Analytical (United Kingdom). Each powdered sample (~10-30 mg) was loaded into an alumina crucible of 100 µl volume and covered with alumina powder almost to the top of the crucible to prevent the oxidation and hydrolysis during the quick transfer to the analyzer and also to avoid a volatile foaming and flowing out of the crucible if the powder sample melted. After loading to the analyzer, each sample was flushed with high purity helium gas (<10 ppm O_2 and H_2O, BIP quality, Air Products) for 90 min and after that heating of sample was performed with the rate of 5°C/min within the pre-determined temperature range. Carrier helium gas flow was set to 28 ml/min. Hydrogen and diborane gas (B_2H_6) levels were measured with the use of mass spectrometer (MS) by analyzing the intensity of ions with the ratio m/z=2 (H_2), 27 (B_2H_6), 26 and 24 (species that may form owing to the decomposition of B_2H_6). For the purpose of graph plotting the measured pressure of escaping gases was normalized by the mass of the powder sample. The mass normalizing was performed to avoid misleading differences in signal intensities caused by different masses of the samples. Such a normalization was reported for the first time in [18] as it

allows a qualitative direct comparison of the peak intensities of various released gases observed on the mass spectrometry (MS) plots that will be discussed in this paper. The measurements were repeated 2-3 times for each sample.

3. Results and discussion

3.1. Microstructure of powders before and after MCAS

SEM micrographs of the morphology of the as-received ultrafine filamentary Ni and graphene additives are shown in Fig. 1a and b, respectively. The agglomerated and entangled filamentary morphology can be clearly seen in the inset micrograph of the Ni additive. However, plate-like graphene powder particles are rather dispersed.

Changing the angular positions of one or two strong NdFeB magnets and altering the number of hard steel balls in a milling vial can control the milling energy in the magneto-ball mill Uni-Ball-Mill 5 [1, 7-10, 24]. As reported recently in [25], the milling energy in the magneto-ball mill Uni-Ball-Mill 5, in particular, the quantity of milling energy, $Q_{TR(R)}$ per unit mass•hour (kJ/gh) injected into and stored in a milled powder for each particular milling mode with a fixed ball-to-powder mass ratio, R, can be calculated via a semi-empirical method. In the present work which used the same milling mode IMP68-4B-R132 for 1h with the constant total milling energy input, Q_{TR}=72.8 kJ/g (Table 5 in Ref. [25]).

Fig. 1c and d show the evolution of the powder morphology for the ($2LiBH_4+MnCl_2$) and (($2LiBH_4+MnCl_2$)+5wt.%Ni) samples, respectively, during ball milling. A refinement of the initial powder mixture with some pronounced agglomerations can be seen in comparison with a large-size of the as-received $LiBH_4$ and $MnCl_2$ particulates, already shown in [8].

3.2. Mechanical dehydrogenation and microstructural evolution of powders during mechano-chemical activation synthesis (MCAS)

The release of small quantities of H_2 during ball milling for the additive-free sample and those with additives was observed. The additive-free sample released about 0.2 wt.% H_2 after 1h BM, which is nearly identical to the amount of H_2 desorbed during BM of the ($nLiBH_4+MnCl_2$) system, previously reported in [8]. Adding 5 wt.% $LiNH_2$ caused a miniscule increase in the desorbed quantity of H_2 to 0.25 wt.% H_2 for (($2LiBH_4+MnCl_2$)+5wt.% $LiNH_2$). The addition of 5 wt.% Ni increased the desorbed quantity of H_2 during BM to 0.48 wt.%.

The sample with 5 wt.% graphene did not exhibit any measurable quantity of mechanical dehydrogenation. A similar mechanical dehydrogenation behavior was observed for the sample

($3LiBH_4+TiF_3$) [26]. We reported that the addition of 5 wt.% graphene resulted in the suppression of mechanical dehydrogenation during the first 3h of milling of a ($3LiBH_4+TiF_3$) powder mixture [26].

Figure 2 shows the XRD patterns of the synthesized ($MnBH_4)_2$/LiCl) samples additive-free and that with 5 wt.% Ni, compared to those after thermal dehydrogenation at 150ºC/20h. The diffraction peaks of $Mn(BH_4)_2$ and LiCl, that are clearly seen after MCAS, confirm that $Mn(BH_4)_2$ was synthesized accompanied by the LiCl by-product as required by reaction Eq. (1). The $Mn(BH_4)_2$ hydride having a trigonal lattice structure (the space group $P3_112$) with the lattice parameters a=10.435(1)Å and c=10.835(2)Å was originally identified by Černý et al. [5] and later confirmed by transmission electron microscopy (TEM) in [9] and XRD [10].

The XRD patterns of the additive-free sample and the one containing 5 wt.% filamentary Ni after thermal dehydrogenation at 150°C in Fig. 2b, d, respectively, clearly show that the $Mn(BH_4)_2$ diffraction peaks are not visible anymore, whereas the LiCl peaks remain very strong. The XRD pattern for a synthesized ($MnBH_4)_2$/LiCl) sample with 5 wt.% graphene in Fig. 3 is nearly identical to that for the additive-free sample.

Figure 4 illustrates the XRD pattern of the 1h BM (($Mn(BH_4)_2$/LiCl)+5 wt.% $LiNH_2$) sample compared to the one after isothermal dehydrogenation at 100°C. The $Mn(BH_4)_2$ and LiCl peaks are observed after mechano-chemical synthesis, whereas the LiCl peaks are the only XRD peaks which can be seen after thermal dehydrogenation.

The XRD results in Fig. 2-4 confirm that the $Mn(BH_4)_2$ diffraction peaks are observed after MCAS and disappear after isothermal dehydrogenation for the ($Mn(BH_4)_2$/LiCl), (($Mn(BH_4)_2$/LiCl)+5 wt.% Ni) and (($Mn(BH_4)_2$/LiCl)+5 wt.% graphene) and (($Mn(BH_4)_2$/LiCl)+5 wt.% $LiNH_2$) samples. Apparently, the formation and thermal decomposition of $Mn(BH_4)_2$ occur through similar paths in both additive-free and additive bearing samples regardless of the type of additive.

3.3. Microstructural evolution of powders after solvent filtration and extraction

Figure 5 illustrates the XRD patterns of synthesized, additive-free ($MnBH_4)_2$/LiCl) after 1st and 2nd EXT at RT (Fig. 5a, b) and at 42°C (Fig. 5c, d), as described in the Experimental section. An XRD pattern of the powder that could not pass through the filter during the solvent filtration and extraction processes is also shown in Fig. 5e. An XRD pattern of the sample after 1st EXT at 42°C and after its isothermal dehydrogenation at 100 ºC is illustrated in Fig. 4f.

From a comparison of the XRD pattern of the sample after MCAS (Fig. 2) with those in Fig. 5, after solvent filtration and extraction, it is seen that new diffraction peaks (triangles) appear in all extracted samples. The same diffraction peaks appear in the XRD patterns after 1st EXT of the powder mixture with the 5 wt.% Ni and graphene additives (Fig. 6a-d). Since the XRD experiments were carried out under exactly the same experimental conditions (see the Experimental) the height of diffraction peaks can be directly compared. Thus, it is clear that the LiCl peaks became weaker (lower intensity) after the1st EXT (Fig. 6a) as compared to the ones after MCAS. The sample after 2nd EXT shows further reduction in the intensity of LiCl peaks (Fig. 6b, d) regardless of the solvent extraction temperature. LiCl is the only phase found in the XRD pattern of the powder inside the filter that could not pass through the filter (Fig. 6e). Figure 6 (e) shows the XRD pattern of the powder remaining inside the filter after the extraction of ($Mn(BH_4)_2$)+5 wt.% Ni) exhibiting the diffraction peaks of Ni. It indicates that filamentary Ni was unable to pass through the filter.

The new diffraction peaks appearing after extraction in Fig. 5 and 6 were identified based on the data reported by Tumanov et al. [16], as corresponding to a dimetallic borohydride solvate [$\{Li(Et_2O)_2\}Mn_2(BH_4)_5$] which has a monoclinic space group C2/c (see Table 2 in [16]). Tumanov et al. [16] studied the reaction of $MnCl_2$ with MBH_4 ($M=Li^+$, Na^+) in Et_2O and reported that [$\{M(Et_2O)_2\}Mn_2(BH_4)_5$] ($M= Li^+$, Na^+) were the crystalline phases identified by XRD.

For the unambiguous identification of [$\{Li(Et_2O)_2\}Mn_2(BH_4)_5$] from the XRD patterns in Fig. 5 and Fig. 6, we used the 2θ values extracted from the synchrotron radiation diffraction pattern reported in [16] for the synthesized powder after reaction of 0.7 g $LiBH_4$ and 2.52 g LiCl in 120 mL Et_2O, which are tabulated in the first column in Table 1. Using the synchrotron 2θ values and the synchrotron radiation wavelength from [16], the plane spacings, $d_{(hkl)}$, for [$\{Li(Et_2O)_2\}Mn_2(BH_4)_5$] were calculated using Bragg's law and are listed in the second column in Table 1. The $d_{(hkl)}$ values experimentally obtained from the XRDs in Fig. 5 are listed in the third column in Table 1. Excellent agreement can be seen from comparison of the plane spacings calculated from the synchrotron radiation (second column) and those from XRD in this work (third column).

Table 1. Experimental 2θ values (from [15]) and calculated lattice spacings, $d_{(hkl)}$ for $[\{Li(Et_2O)_2\}Mn_2(BH_4)_5]$ from synchrotron radiation, calculated $d_{(hkl)}$ X-ray radiation from this work.

Experimental 2θ values from synchrotron radiation (λ=0.82742 Å) pattern in [16]	**Calculated $d_{(hkl)}$ (Å) for $[\{Li(Et_2O)_2\}Mn_2(BH_4)_5]$ from the Bragg's law using λ=0.82742 Å for synchrotron radiation**	**Experimental $d_{(hkl)}$ (Å) from XRD patterns Fig. 5**
4.701	10.0874	---
6.582	7.2066	---
7.209	6.5805	6.5838
7.925	5.9868	6.0212
9.000	5.2629	5.2593
9.403	5.0874	5.0914
9.940	4.7754	4.8049
10.836	4.3815	4.3771
12.000	3.9579	3.9877
12.269	3.8714	3.8842
12.537	3.7889	3.8010
13.746	3.4571	3.4740
14.194	3.3485	3.3581
15.537	3.0806	3.0984
15.806	3.0089	3.0242
16.075	2.9589	---
16.612	2.8638	2.8631

The finding of $[\{Li(Et_2O)_2\}Mn_2(BH_4)_5]$ after the solvent extraction of the mechano-chemically synthesized, solid state $Mn(BH_4)_2$/LiCl mixture, is the most striking result obtained in this work, that has never been reported in the literature. This behavior is opposite to the results of our recent study [18], where we investigated a mechano-chemical synthesis of a $Mn(BH_4)_2$/NaCl mixture during ball milling of the ($2NaBH_4$+$MnCl_2$) i.e. when $LiBH_4$ is replaced by $NaBH_4$ in Eq. (1) and (3). We reported in [18] that the process of solvent extraction at 42°C, causing removal of the "dead-weight" NaCl by-product from the mixture, resulted in the transformation of the amorphous $Mn(BH_4)_2$-type hydride, synthesized by MCAS, into its crystalline form after extraction.

Figure 7a shows an SEM micrograph of ($Mn(BH_4)_2$)/LiCl) after 1st EXT at 42°C (the corresponding XRD pattern is shown in Fig. 5a). An SEM micrograph of ($Mn(BH_4)_2$)/LiCl)+5 wt.% Ni) extracted at 42° (1st EXT) is shown in Fig. 7b (see a corresponding XRD pattern in Fig. 6 (c)). The morphology of the powder remaining in the filter after solvent extraction for

($Mn(BH_4)_2$)+5 wt.% Ni) is shown in Fig. 7c. Its corresponding XRD pattern is shown in Fig. 6 (e).

The presence of Ni might have improved the kinetics of dehydrogenation in the extracted samples. Unfortunately, we were unable to obtain the Ni additive in the extracted sample since, as detected by XRD in Fig. 6(c) and (e), filamentary Ni could not pass through the filter and remained in it. We originally expected that filamentary Ni would pass through the filter due to its filament size smaller than the filter mesh size (Fig. 1a). However, as illustrated in an SEM micrograph in Fig. 7c, the morphology of Ni, remaining in the filter, consists of severely entangled filaments of Ni which is a very similar morphology to the as received filamentary Ni in Fig. 1a. It seems that despite a heavy ball milling process, the initial Ni morphology is not completely destroyed into smaller filaments and, hence, the Ni agglomerates were not able to pass through the filter used in the solvent extraction.

Fig. 5 shows that the low intensity LiCl peaks can still be seen even after filtration/extraction. There are two likely explanations for this observation: (1) although LiCl is extremely poorly soluble in pure Et_2O, it can be efficiently trapped by the [$Mn(BH_4)_2$-Et_2O] system, consequently increasing the solubility and (2) LiCl particles smaller in size than the filter mesh size (0.2μm) may have formed and, therefore, cannot be completely filtered out.

3.4. FT-IR analysis of all samples

The reference FT-IR spectrum for a synthesized ($Mn(BH_4)_2$/LiCl) sample is shown in Fig. 8a (adapted from [8]). The FT-IR spectra for the synthesized (($Mn(BH_4)_2$/LiCl)+5wt.% $LiNH_2$) sample and the additive-free [{$Li(Et_2O)_2$}$Mn_2(BH_4)_5$]/LiCl sample obtained after 1st EXT are shown in Fig. 8b and c, respectively. The FT-IR spectra shown in Fig. 8b strongly support the presence of $Mn(BH_4)_2$ in this sample. Two IR active modes of B-H bending in the range of 1050-1350 cm^{-1} and stretching in the range of 2150-2400 cm^{-1} [8, 27] are visible in the FT-IR spectrum of the ball milled sample. The bending and stretching bond of B-H formed after synthesis of ($Mn(BH_4)_2$/LiCl)+5 wt.% $LiNH_2$) in Fig. 8b compares favorably to the reference FT-IR spectrum for the crystalline $Mn(BH_4)_2$ in Fig. 8a. It is worth noting that the N-H stretch bond in pure $LiNH_2$ is within the wave number range of 3500-3700 cm^{-1} but it is shifted to the higher wave number of 3290-3360 cm^{-1} by adding 5 wt.% $LiNH_2$ (Fig. 8b). A similar result was observed by Song et al. [11].

Furthermore, two IR characteristic bands for the BH_4^- groups within the ranges 1050-1350 cm^{-1} and 2150-2400 cm^{-1} in Fig. 8c strongly support the presence of borohydride in the sample extracted at 42ºC. The modes of C-H bending in the range of 750-900 cm^{-1} and stretching within the ranges 1390-1470 and 2900-2980 cm^{-1} and the typical C-O-C stretch band in the range of 1000-1090 cm^{-1}, exhibit a set of characteristic bands for the Et_2O molecules (Fig. 8c) as reported in [16, 28].

3.5. Gas mass spectrometry (MS) and **DSC/TGA** *thermal behavior of ball milled and solvent extracted samples*

Figure. 9a, b shows the MS and DSC/TGA results, respectively, for the synthesized, additive-free, ($Mn(BH_4)_2$/LiCl) sample. Fig. 9c, d shows the MS and DSC/TGA results, respectively, for (($Mn(BH_4)_2$/LiCl)+5wt.% graphene). Fig. 9e, f shows the MS and DSC/TGA results, respectively, for the (($Mn(BH_4)_2$/LiCl)+5 wt.% $LiNH_2$) sample. Fig. 9g, h shows the MS and DSC/TGA thermal results, respectively, for the synthesized (($Mn(BH_4)_2$/LiCl)+5wt.% Ni) sample. The broken red line in Fig. 9b, d, f, h shows a first derivative of the TG line (dTG/dT where T-temperature). It very precisely indicates the range of temperatures within which the mass loss occurs and clearly confirms that the TG mass loss in Fig. 9b, d, f, h is, indeed, corresponds to the occurrence of DSC peaks.

It has been reported that some quantities of diborane gas (B_2H_6) are usually released during thermal decomposition of $Mn(BH_4)_2$ [10-11]. Most interestingly, Varin et al. [10] reported that the MS peak intensity of the H_2 released from $Mn(BH_4)_2$, mechano-chemically synthesized by ball milling in a magneto-mill, was several hundred times bigger than that of B_2H_6 gas, which was also released together with H_2.

The release of H_2 as a principal gas accompanied by a very small quantity of diborane, B_2H_6, is observed for all five samples in Fig. 9a, c, e, g. Hydrogen release started at 100°C, with a maximum intensity at around 140-160 °C. The MS peak area intensity ratio H_2/B_2H_6 is 493 up to 200°C for the ($Mn(BH_4)_2$/LiCl) sample (Fig. 9 (a)) and increases to 722 by adding 5 wt.% graphene (Fig. 9 (c)). This clearly indicates that graphene reasonably effectively reduces the release of B_2H_6. Fig. 9(e) shows the MS peak area intensity ratio H_2/B_2H_6=3213 for the (($Mn(BH_4)_2$/LiCl)+5 wt.% $LiNH_2$) powder mixture. Gas mass spectrometry of the sample with 5 wt.% Ni (Fig. 9g), however, shows even more greatly suppressed B_2H_6 (H_2/B_2H_6=4667).

It is apparent from the dynamic dehydrogenation experiments that using 5 wt.% of each additives can minimize the released quantity of B_2H_6 during dehydrogenation of synthesized $Mn(BH_4)_2$, increasing the released peak area intensity ratio H_2/B_2H_6 up to 200°C from 493 for an additive-free sample (Fig.9a), to 722 for 5 wt. % graphene (Fig.9c), to 3213 for 5 wt.% $LiNH_2$ (Fig. 9e) and to 4667 for 5 wt.% Ni (Fig. 9g). It seems that the additives of filamentary Ni and $LiNH_2$ suppress the release of B_2H_6 from synthesized, crystalline $Mn(BH_4)_2$ much more effectively than graphene.

Song et al. [11] studied the release of H_2 and B_2H_6 from the BM mixture $3LiBH_4/MnF_2$. They suggested that adding 2.5 wt.% $LiNH_2$ could suppress the release of B_2H_6, and indeed, no trace of B_2H_6 was observed when the quantity of $LiNH_2$ reached 5 wt.%. They suggested that the $LiNH_2$ improvements were attributed mainly to the destabilization of B-H bonds in borohydride and the prevention of the formation of B-H-B bonds for B_2H_6 by the interaction of BH_4^- and NH_2^-. Apparently, following Song et al. [11], one could argued that filamentary Ni also prevents the formation of B-H-B bonds for B_2H_6, perhaps, even more effectively than $LiNH_2$ albeit by a different mechanism, elucidation of which needs more studies. Alternatively, Desrosiers et al. [29] reported that at low gas exposures and heating to 500 K resulted in complete decomposition of B_2H_6, leaving B bonded to the Ni(100) surface. More recently, we proposed that $LiNH_2$ reacts with B_2H_6 in an exothermic reaction during desorption, resulting in the formation of either lithium hydride or lithium borohydride accompanied by boron nitride [30].

The DSC curve of the ($Mn(BH_4)_2$/LiCl) sample (Fig. 9b) exhibits a strong endothermic peak with the maximum at around 150°C. The principal endothermic peak and its maximum is slightly shifted to a higher temperature range (maximum at 168°C) by adding 5 wt.% graphene (Fig. 9d). In contrast, the DSC peak of the sample with 5 wt.% Ni is slightly shifted to a lower temperature, with the maximum at about 146°C (Fig. 9h). Therefore, the release of H_2 gas containing a small amount of B_2H_6 in Fig. 9a, c, g, is an endothermic event resulting in some mass loss up to about 200°C.

Fig. 9f shows the DSC curve of the sample with 5 wt.% $LiNH_2$; a pronounced exothermic peak (120ºC) before the characteristic endothermic peak for decomposition of $Mn(BH_4)_2$ at (133ºC) indicates that the decomposition mechanism of this sample most likely differs from the other additive-free sample and the samples containing graphene and filamentary Ni.

It is to be pointed out that while the addition of filamentary Ni greatly reduces the release of B_2H_6 it does not reduce the decomposition temperature of $Mn(BH_4)_2$. On the other hand, the second strongest reducer of B_2H_6, $LiNH_2$, also reduces the decomposition temperature of $Mn(BH_4)_2$, as shown by the endothermic peak in DSC, from about 150-160°C (Fig. 9b, d, h) to 133 °C (Fig. 9f). Song et al. [11] reported that a significant decrease in the decomposition temperature of $Mn(BH_4)_2$ synthesized from a mixture of $LiBH_4$ and MnF_2 such that 5 wt.% $LiNH_2$ reduced the decomposition temperature from 138ºC for an un-doped sample to 111ºC for the one with 5 wt.% $LiNH_2$. However, they mentioned that using $LiNH_2$ did not improve the kinetic of dehydrogenation of the synthesized material. They also reported that in comparison to pure $LiNH_2$, the characteristic peaks of the N-H stretch bonds in the $LiNH_2$-doped $3LiBH_4/MnF_2$ composites shifted towards higher wavenumbers, which suggested that the combination of BH_4^- and NH_2^- has taken place during the doping process.

In contrast, in Fig. 9d, 5 wt.% graphene increases the DSC decomposition peak temperature of $Mn(BH_4)_2$ from about 150°C (Fig. 9b) to about 168 °C.

Based on the results of mechano-chemical synthesis and thermal decomposition for $Mn(BH_4)_2$, additive-free and with the additives of graphene, filamentary Ni and $LiNH_2$, discussed in Sec. 3.2 and 3.5, we suggest that the dehydrogenation/decomposition reaction for the mechano-chemically synthesized $Mn(BH_4)_2/LiCl$, regardless of the nature of an additive, can be presented in the following general form:

$$2LiBH_4+MnCl_2 \rightarrow BM \rightarrow Mn(BH_4)_2+2LiCl \rightarrow Temp \rightarrow Mn+xB_2H_6+yB+zH_2+[2LiCl] \quad (3)$$

Unfortunately, the estimate of the exact values of x, y, z is rather difficult although taking into account very high ratios H_2/B_2H_6 in Fig. 9a, c, e, g, most likely $x<<z$. Furthermore, the suggested general dehydrogenation reaction (3) requires the formation of the elemental Mn and B species. The Mn diffraction peaks are not observed in the present work in Fig. 2-4 in the XRD patterns after dehydrogenation of $Mn(BH_4)_2$ and have not been observed in the previous works [7, 8, 10]. That strongly suggests, at the first look, that Mn and B could be amorphous or highly nanocrystalline after decomposition of $Mn(BH_4)_2$. For example, we reported [9] that, in reality, both nanocrystalline Mn and B existed in the dehydrogenated powder by using SADP and energy-dispersive X-ray spectroscopy (EDS) for the ($Mn(BH_4)_2/LiCl$) sample after synthesis and subsequent isothermal dehydrogenation at 100°C.

Figure 10a-d shows the MS and TGA/DSC curves, respectively, for two repeated samples without additive, containing [{Li(Et_2O)$_2$}$Mn_2(BH_4)_5$] as a principal hydride phase and some retained LiCl (Fig. 5a-d), which were obtained after 1st EXT. The MS curve for the first sample in Fig. 10a shows a narrow H_2 peak doublet while the second sample in Fig. 10c shows a single, smooth, H_2 peak. Both samples also show peaks of released B_2H_6. Remarkably, the calculated MS peak area intensity ratio H_2/B_2H_6 is nearly identical for both samples being equal to 147 and 148 for samples in Fig. 10a and b, respectively. This ratio is lower than that for the additive-free $Mn(BH_4)_2$/LiCl sample in Fig. 9a which indicates a higher quantity of B_2H_6 released from solvent extracted ([{Li(Et_2O)$_2$}$Mn_2(BH_4)_5$]/LiCl) than that released from mechano-chemically synthesized $Mn(BH_4)_2$/LiCl in dynamic decomposition experiments in a TG apparatus under a continuous flow of helium gas.

The DSC curves in Fig. 10b, d show endothermic doublet peak for both samples with the respective DSC peaks at 100 and 150°C. A first derivative of the TG line (dTG/dT-broken red line) confirms the exact positions of DSC peaks. The TG analysis shows that the first sample exhibits at least three distinctive mass loss steps designated 1, 2 and 3 in Fig. 10b. In step 1 the mass loss reaches about 39% up to 150°C. In the next steps 2 and 3 up to 300°C the mass loss amounts to about 6%. The TG curve for the second sample in Fig. 9d contains only two steps of mass loss where in step 1 the mass loss reaches about 40% up to 150°C and ~5 % in step 2 up to 300°C. In the middle of step 1 there seems to appear a slight inflection point on the TG line (at ~120°C) which might be related to a beginning of H_2 desorption simultaneous with decomposition of Et_2O.

As mentioned earlier, Tumanov et al. [16] synthesized [{Li(Et_2O)$_2$}$Mn_2(BH_4)_5$] accompanied by LiCl from the wet metathesis reaction between $MnCl_2$ and $LiBH_4$ in Et_2O. They studied its thermal properties during dynamic decomposition in a TG apparatus under argon atmosphere. They found that [{Li(Et_2O)$_2$}$Mn_2(BH_4)_5$] decomposed in three defined steps. The first step up to about 110°C, exhibiting a mass loss of ~26.8% was assigned to the evolution of Et_2O while the second mass loss of ~5.2% up to about 160°C, was assigned to the decomposition of $Mn(BH_4)_2$. The nature of the third step up to ~325°C was not explained by the authors.

It is clear that our TG results in Fig. 10b, d are in disagreement with those reported by Tumanov et al. [16]. One of the discrepancies is the quantity of mass loss observed in step 1 in Fig. 9b, d which amounts to ~40% vs. only ~27% reported by Tumanov et al. [16]. It can be calculated that

the theoretical capacity of Et_2O in $[\{Li(Et_2O)_2\}Mn_2(BH_4)_5]$ is 43.7 wt.% and the theoretical capacity of H_2 is ~5.9 wt. % (the practical values are slightly lower due to the presence of LiCl co-existing with $[\{Li(Et_2O)_2\}Mn_2(BH_4)_5]$ after solvent extraction as can be seen in Fig. Fig. 5f and 6d).

As such, the observed mass loss of ~40% in step 1 in Fig. 10b, d agrees quite well with a theoretical capacity of Et_2O in $[\{Li(Et_2O)_2\}Mn_2(BH_4)_5]$ corrected for the presence of LiCl. Furthermore, the mass loss in step 2 and 3 in Fig. 10b and step 2 in Fig. 10d, can be assigned to the desorption of H_2 (mixed with B_2H_6) from $[\{Li(Et_2O)_2\}Mn_2(BH_4)_5]$ according to a hypothetical decomposition reaction:

$$[\{Li(Et_2O)_2\}Mn_2(BH_4)_5]+[\text{retained LiCl}]\rightarrow Li+2Et_2O+2Mn+xB_2H_6+yB+zH_2+[\text{retained LiCl}] \quad (4)$$

Reaction Eq. (4) correlates well with the XRD patterns in Fig. 5f and 6d showing the microstructure after a complete isothermal decomposition of $[\{Li(Et_2O)_2\}Mn_2(BH_4)_5]$ with the sole diffraction peaks of the retained LiCl visible. Similarly to dehydrogenation reaction (3) for $Mn(BH_4)_2$, reaction (4) requires the formation of the elemental Mn and B species whose diffraction peaks are not observed in Fig. 5f and 6d, most likely, due to either their amorphous or highly nanocrystalline structure [9].

3.6. Isothermal dehydrogenation of the ball milled and solvent extracted samples

Figure 11 shows the isothermal dehydrogenation curves at 100°C under 1 bar H_2 pressure for an additive-free sample (a light blue curve) and for samples containing 5 wt.% of filamentary Ni, graphene and $LiNH_2$. It is observed that the additive of graphene makes dehydrogenation quite sluggish while the $LiNH_2$ additive seems to accelerate dehydrogenation. The filamentary Ni additive seems to be neutral. As mentioned earlier, the theoretical capacity of reaction (1) for n=2 is 4.76 wt.% H_2 for a mixture of synthesized $Mn(BH_4)_2$ and LiCl, which will be reduced to 4.53 wt.% H_2 by adding 5 wt.% additive to the as-received materials and further reduced slightly by a quantity of released B_2H_6 as in reaction Eq. (3). After 20h of desorption (Fig. 11) the total quantity of desorbed hydrogen at 100°C is fluctuating around 4 wt.% with the exception of the sample with 5 wt.% graphene which exhibits a slightly lower value of 3.8 wt.% H_2.

Figure 12a, b, c shows an example of the Arrhenius plots of rate constant k with temperature (100, 150 and 200°C) for estimation of the apparent activation energy of hydrogen desorption for three samples of 1h synthesized $(Mn(BH_4)_2)$/LiCl)+5 wt.% $LiNH_2$). All three plots exhibit a very low apparent activation energy with excellent coefficients of determination R^2.

Similar Arrhenius plots were constructed for the additive-free ($Mn(BH_4)_2$/LiCl) samples and the synthesized samples with the graphene and filamentary Ni additives at three temperatures of 100, 150 and 200 ºC from which the apparent activation energies for dehydrogenation were estimated and are shown by bar graph in Fig. 12d, including the one for the $LiNH_2$ additive. As shown in Fig. 12d, as compared to 78.9±1.2 kJ/mol for the additive-free ($Mn(BH_4)_2$/LiCl) sample, the activation energy of 76.1±0.6 kJ/mol for a 5 wt.% Ni-bearing ($Mn(BH_4)_2$/LiCl) sample indicates that 5 wt.% Ni yields no obvious improvement in the kinetic of dehydrogenation. Graphene, however, has a slightly higher apparent activation energy for dehydrogenation (81.5±5.2 kJ/mol), which was expected since (($Mn(BH_4)_2$/LiCl)+5 wt.% graphene) shows slow dehydrogenation at 100ºC compared to other samples as illustrated in Fig. 11. The most notable observation emerging from the apparent activation energy comparison is that 5 wt.% $LiNH_2$ can reduce the apparent activation energy to 44.9±4.3 kJ/mol. This reduction may result from the destabilizing of the B-H bonds in the synthesized $Mn(BH_4)_2$/LiCl mixture through the electrostatic attraction between H^- in BH_4^- and H^+ in NH_2^-, with consequently lower decomposition temperature and faster dehydrogenation as reported in [11].

Figure 13a, b shows the isothermal volumetric H_2 desorption curves under 1 bar H_2 pressure at 100 and 200°C, respectively, for a dimetallic borohydride solvate, [{$Li(Et_2O)_2$}$Mn_2(BH_4)_5$]/LiCl, obtained after 1st and 2nd extraction at 42°C (1st EXT&2nd EXT). In general, there is no drastic difference in a shape of desorption curves after 1st and 2nd EXT. After 20 h of desorption, a dimetallic borohydride solvate desorbed about 5 and 5.5 wt.% H_2 at 100 and 200°C, respectively, which correlates with the observed mass loss in a TG apparatus in step 2 and 3 in Fig. 10b and step 2 in Fig. 10d. This finding indicates that the quantity of desorbed B_2H_6 observed in MS in Fig. 10a,c, in a dynamic decomposition event, did not substantially affect the quantity of H_2 desorbed isothermally at 100 and 200°C in Fig. 13. Hypothetically, during decomposition in isothermal conditions under 1 bar H_2, the quantity of B_2H_6 in reaction Eq. (4) might be much smaller than that during a dynamic decomposition in a TG apparatus under a constant flow of helium gas. This interesting problem needs more complex studies involving a combined isothermal decomposition with a simultaneous mass spectrometry (MS) of released gases which is beyond the scope of this study. Furthermore, the notion that the observed mass loss after the Et_2O decomposition in step 2 and 3 (Fig. 10b) and step 2 (Fig.10d) is due to the H_2 released from decomposing [{$Li(Et_2O)_2$}$Mn_2(BH_4)_5$] is qualitatively supported by the results in Fig. 13.

4. Conclusions

1) A crystalline $Mn(BH_4)_2$ hydride together with a by-product LiCl salt were synthesized in the ($2LiBH_4+MnCl_2$) powder mixtures, without additives and with additives such as 5 wt.% of ultrafine filamentary carbonyl nickel, graphene and $LiNH_2$, by mechano-chemical activation synthesis (MCAS) (metathesis reaction) for 1 h in a magneto-ball mill.

2) During 1h BM the additive-free sample released by mechanical-dehydrogenation about 0.2 wt.% H_2 and those with 5 wt.% $LiNH_2$ and filamentary Ni released 0.25 and 0.48 wt.% H_2, respectively.

3) The sample with 5 wt.% graphene did not exhibit any measurable mechanical dehydrogenation.

4) It was found for the first time that during dynamic dehydrogenation of the synthesized ($Mn(BH_4)_2$/LiCl) mixture up to 200°C in TGA/MS, each additive reduced the released quantity of B_2H_6, increasing the released MS gas intensity ratio H_2/B_2H_6 from 493 for an additive-free sample, to 4667 for 5 wt.% filamentary Ni, to 3213 for 5 wt.% $LiNH_2$ and to 722 for 5 wt. % graphene. Apparently, the filamentary Ni additive is the most effective suppressor of B_2H_6 released from crystalline $Mn(BH_4)_2$.

5) The addition of 5 wt.% of $LiNH_2$ reduced the decomposition maximum peak temperature of $Mn(BH_4)_2$, characterized by an endothermic peak in DSC, from 150°C to 133°C, while filamentary Ni did not reduce the decomposition temperature of $Mn(BH_4)_2$. The addition of 5 wt.% graphene slightly increased the DSC decomposition maximum peak temperature of $Mn(BH_4)_2$ from about 150°C to168 °C.

6) The DSC curve of the BM (($Mn(BH_4)_2$/LiCl)+5 wt.% $LiNH_2$) sample shows a pronounced exothermic peak with a maximum at 120ºC preceding the characteristic endothermic peak with a maximum at 133ºC corresponding to the decomposition of $Mn(BH_4)_2$.

7) The apparent activation energy of 78.9±1.2 kJ/mol and 76.1±0.6 kJ/mol for the additive-free sample and the 5 wt.% Ni-bearing sample, respectively, are quite similar. The addition of 5 wt.% of graphene, slightly increased the apparent activation energy for dehydrogenation to 81.5±5.2 kJ/mol. Most importantly, 5 wt.% $LiNH_2$ greatly reduced the apparent activation energy to 44.9±4.3 kJ/mol.

8) The most striking result, that has never been reported in the literature, is that during a process of solvent extraction of the mechano-chemically synthesized ($Mn(BH_4)_2$+LiCl) sample, a

dimetallic borohydride solvate, [{Li(Et_2O)$_2$}$Mn_2(BH_4)_5$], crystallized instead of crystalline $Mn(BH_4)_2$.

9) During dynamic thermal decomposition in a DSC/TG apparatus under a flow of helium, a dimetallic borohydride solvate, [{Li(Et_2O)$_2$}$Mn_2(BH_4)_5$], decomposed within the range of 50-300°C, exhibiting a loss of about 40 wt.% diethyl ether (Et_2O), 5-6 wt.% H_2 and some quantity of B_2H_6.

10) Volumetric isothermal desorption of [{Li(Et_2O)$_2$}$Mn_2(BH_4)_5$], under 1 bar H_2 pressure, resulted in about 5 and 5.4 wt.% H_2 desorbed within ~20h at 100°C and 200°C, respectively.

Acknowledgments

This research was supported by a Natural Sciences and Engineering Research Council (NSERC) of Canada Discovery grant to Prof. R.A. Varin which is gratefully acknowledged. The authors are grateful to Prof. Linda Nazar from the Department of Chemistry, University of Waterloo, for allowing access to XRD equipment. The authors thank Dr. Steve Kornic from McMaster University for conducting the FT-IR analysis. The authors also thank Dr. John Shu (CEO) from Cnem Corp. Canada for donating ultrafine filamentary carbonyl Ni.

References

[1] R.A. Varin, T. Czujko, Z.S. Wronski. Nanomaterials for solid state hydrogen storage. New York, Springer Science, 2009. Business Media.

[2] R.A. Varin, Z.S. Wronski. Progress in hydrogen storage in complex hydrides, Ch.13, pp. 293-332, in Renewable Hydrogen Technologies. Production, Purification, Storage, Applications and Safety, Eds. Gandia LM, Arzamendi G, Diéguez PM, Elsevier, 2013 (ISBN: 978-0-444-56352-1).

[3] R.A. Varin, A.R. Shirani Bidabadi. Nanostructured, complex hydride systems for hydrogen generation. AIMS Energy 3 (2015) 121-143.

[4] P. Choudhury, S.DS. Srinivasan, V.R. Bhethanabotla, Y. Goswami, K. McGrath, E.K. Stefanakos. Nano-Ni doped Li-Mn-B-H system as a new hydrogen storage candidate. Int J Hydrogen Energy 34 (2009) 6325–34.

[5] R. Černý, N. Penin, H. Hagemann, Y. Filinchuk. The first crystallographic and spectroscopic characterization of a 3d-metal borohydride: $Mn(BH_4)_2$. J Phys Chem C 113 (2009) 9003–9007.

[6] R. Liu, D. Reed, D. Book. Decomposition behaviour of $Mn(BH_4)_2$ formed by ball-milling $LiBH_4$ and $MnCl_2$. J Alloys Compd 515 (2012) 32-38.

[7] R.A. Varin, L. Zbroniec. The effects of ball milling and nanometric nickel additive on the hydrogen desorption from lithium borohydride and manganese chloride ($3LiBH_4+MnCl_2$) mixture. Int J Hydrogen Energy 35 (2010) 3588-97.

[8] R.A. Varin, A.R. Shirani Bidabadi. The effect of milling energy input during mechano-chemical activation synthesis (MCAS) of the nanocrystalline manganese borohydride ($Mn(BH_4)_2$) on its thermal dehydrogenation properties. Int J Hydrogen Energy 2014; 39: 11620-11632.

[9] A. R Shirani Bidabadi, A. Korinek, G A. Botton, R.A. Varin. High resolution transmission electron microscopy (TEM), energy-dispersive X-ray spectroscopy (EDS) and X-ray diffraction studies of nanocrystalline manganese borohydride ($Mn(BH_4)_2$) after mechano-chemical synthesis and thermal dehydrogenation. Acta Mater 2015; 100: 392-400.

[10] R.A. Varin, L. Zbroniec, M. Polanski, Y. Filinchuk, R. Černý. Mechano-chemical synthesis of manganese borohydride ($Mn(BH_4)_2$) and inverse cubic spinel (Li_2MnCl_4) in the ($nLiBH_4+MnCl_2$) (n=1, 2, 3, 5, 9 and 23) mixtures and their dehydrogenation behavior. Int J Hydrogen Energy 37 (2012) 16056-16069.

[11] Yun Song, Fang Fang, Yongtao Li, Qiyang Zhao, Dalin Sun, Qingan Zhang, Liuzhang Ouyang, Min Zhu. Promoted hydrogen release from $3LiBH_4/MnF_2$ composite by doping $LiNH_2$: Elimination of diborane release and reduction of decomposition temperature. Int J Hydrogen Energy 37 (2012) 18074-18079.

[12] M. Fichtner, O. Fuhr. Synthesis and structures of magnesium alanate and two solvent adducts. J Alloys Compd 345 (2002) 286-296.

[13] T.D. Humphries TD, Ley MB, Frommen C, K.T. Munroe, Jensen TR, Hauback BC. Crystal structure and in situ decomposition of $Eu(BH_4)_2$ and $Sm(BH_4)_2$. J. Matter. Chem A 2015; 3: 691-698.

[14] K. Chłopek, C. Frommen, A. Le´on, O. Zabara, M. Fichtner. Synthesis and properties of magnesium tetrahydroborate $Mg(BH_4)_2$. Journal of Materials Chemistry 17 (2007) 3496-3503.

[15] B. Richter, D.B. Ravnsbæk, N.A. Tumanov, Y. Filinchuk, T.R. Jensen. Manganese borohydride; synthesis and characterization. Dalton Transactions 44 (2015) 3988-3996.
[16] N.A. Tumanov, D.A. Safin, B. Richter, Z. Łodziana, T.R. Jensen, Y. Garcia, Y. Filinchuk. Challenges in the synthetic routes to $Mn(BH_4)_2$: insight into intermediate compounds. Dalton Transactions 44 (2015) 6571-6580.
[17] M. Mamatha, B. Bogdanović, M. Felderhoff, A. Pommerin, W. Schmidt, F. Schüth, C. Weidenthaler. Mechanochemical preparation and investigation of properties of magnesium, calcium and lithium–magnesium alanates. J Alloys Compd 407 (2006) 78-86.
[18] R.A. Varin, D.A. Mattar, A.R. Shirani Bidabadi, M. Polanski. Synthesis of amorphous manganese borohydride in the ($NaBH_4$–$MnCl_2$) system, its hydrogen generation properties and crystalline transformation during solvent extraction. J Energy Chemistry 26 (2017) 24-34.
[19] A. Calka, A.P. Radlinski. Universal high performance ball-milling device and its application for mechanical alloying. Mater Sci Eng A 134 (1991) 1350-1353.
[20] Patents: WO9104810, US5383615, CA2066740, EP0494899, AU643949.
[21] A. Calka, R.A. Varin. Application of Controlled Ball Milling in Materials Processing. In: Srivatsan TS, Varin RA, Khor M, editors. Int. Symp. on Processing and Fabrication of Advanced Materials IX (PFAM IX). ASM International: Materials Park, OH, 2001. p. 263-287.
[22] R.A. Varin, S. Li, Z. Wronski, O. Morozova, T. Khomenko. The effect of sequential and continuous high-energy impact mode on the mechano-chemical synthesis of nanostructured complex hydride Mg_2FeH_6. J. Alloys Compd. 390 (2005) 282–296 .
[23] G. Sandrock, K. Gross, G. Thomas, C. Jensen, D. Meeker, S. Takara. Engineering considerations in the use of catalyzed sodium alanates for hydrogen storage. J Alloys Compd. 330-332 (2002) 696-701.
[24] R.A. Varin, R. Parviz. The effects of the micrometric and nanometric iron (Fe) additives on the mechanical and thermal dehydrogenation of lithium alanate ($LiAlH_4$), its self-discharge at low temperatures and rehydrogenation. Int J Hydrogen Energy 37 (2012) 9088-9102.
[25] R. Parviz, R.A. Varin. Combined effects of molar ratio and ball milling energy on the phase transformations and mechanical dehydrogenation in the lithium amide-magnesium hydride ($LiNH_2$+$nMgH_2$)(n=0.5-2.0) nanocomposites. Int J Hydrogen Energy 38 (2013) 8313-8327.

[26] A.R. Shirani Bidabadi, R.A. Varin, M. Polanski, L. Stobinski. Mechano-chemical activation of the ($3LiBH_4+TiF_3$) system, its dehydrogenation behavior and the effects of ultrafine filamentary Ni and graphene additives. RSC Advances 6 (2016) 93245-93258.

[27] R.A. Varin, A.R. Shirani Bidabadi. Rapid, ambient temperature hydrogen generation from the solid state Li-B-Fe-H system by mechano-chemical activation synthesis. J. Power Sources 284 (2015) 554-565.

[28] http://www.ochemonline.com/Infrared_spectroscopy_absorption_table

[29] R.M. Desrosiers, D.W. Greve, A.J. Gellman. Decomposition of B_2H_6 on Ni (100). J Vac Sci Technol A: Vac. Surfaces Films 15 (1997) 2181.

[30] R.A. Varin, D.K. Mattar, M. Polanski, A.R. Shirani Bidabadi, L. Stobinski. The effects of additives on the dehydrogenation of amorphous manganese borohydride and its crystalline form after solvent filtration/extraction. Energies 10 (2017) 1741.

Figure captions

Fig. 1. Scanning electron micrographs of (a) as received ultrafine filamentary Ni (b) as received graphene (flake-reduced graphene oxide-(FL-rGO)), (c) 1h ball milled ($2LiBH_4+MnCl_2$) mixture and (d) 1h BM (($2LiBH_4+MnCl_2$)+5 wt.% Ni) mixture.

Fig. 2. XRD patterns of the ($2LiBH_4+MnCl_2$) powder mixture after: (a) 1h BM and (b) isothermal dehydrogenation at 150 °C. The (($2LiBH_4+MnCl_2$)+5 wt.% Ni) sample after: (c) 1h BM and (d) after isothermal dehydrogenation at 150°C.

Fig. 3. XRD patterns of the mixture (($2LiBH_4+MnCl_2$)+5 wt.% graphene) ball milled for 1h (Q_{TR}=72.8 kJ/g) and after dehydrogenation at 150°C.

Fig. 4. XRD patterns of the mixture (($2LiBH_4+MnCl_2$)+5 wt.% $LiNH_2$) ball milled for 1h (Q_{TR}=72.8 kJ/g) and after dehydrogenation at 100°C.

Fig. 5. XRD patterns of synthesized ($Mn(BH_4)_2$)/LiCl) after a) first solvent extraction at room temperature (RT), b) second solvent extraction at RT, c) first solvent extraction (1^{st} EXT) at 42°C, d) second solvent extraction (2^{nd} EXT) at 42°C. e) Powder remaining in the filter after 1^{st} EXT at 42°C. f) Powder after 1^{st} EXT subsequently isothermally dehydrogenated at 100°C under 1 bar H_2 pressure.

Fig. 6. XRD patterns of a) (($2LiBH_4+MnCl_2$)+5 wt.% graphene)-1h BM extracted at 42°C, b) after dehydrogenation at 200 °C, c) (($2LiBH_4+MnCl_2$) +5 wt.% Ni)-1h BM and extracted at 42°C, d) sample in c) after dehydrogenation at 200 °C under 1 bar H_2, and e) powder in the filter through extraction of sample c).

Fig. 7. SEM micrograph of (a) ($Mn(BH_4)_2$)/LiCl) extracted at 42°C (b) (($Mn(BH_4)_2$)/LiCl)+5 wt.% Ni) extracted at 42°C, (c) powder left in the filter during the solvent extraction process of the (($Mn(BH_4)_2$)/LiCl)+5 wt.% Ni) sample.

Fig. 8. (a) Reference FT-IR spectrum for a synthesized ($Mn(BH_4)_2$)/LiCl) sample (adapted from [8]), (b) FT-IR spectrum for a synthesized (($Mn(BH_4)_2$)/LiCl)+5 wt.% $LiNH_2$) sample and (c) FT-IR spectrum for a synthesized ($Mn(BH_4)_2$)/LiCl) sample after 1st EXT at 42°C.

Fig. 9. a) Mass spectroscopy (MS) and b) TG and DSC curves, respectively, for a synthesized $Mn(BH_4)_2$/LiCl sample. c) MS and d) TG and DSC curves, respectively, for synthesized ($Mn(BH_4)_2$/LiCl+5 wt.% graphene). e) MS and f) TG and DSC curves, respectively, for synthesized ($Mn(BH_4)_2$/LiCl)+5 wt.% $LiNH_2$). g) MS and h) TG and DSC curves, respectively, for a synthesized (($Mn(BH_4)_2$)/LiCl)+5 wt.% Ni) sample. Peak area intensity ratios H_2/B_2H_6 are indicated.

Fig. 10. a) MS gas desorption spectra (not normalized by the mass of the powder sample) and b) TG and DSC curves for ([{$Li(Et_2O)_2$}$Mn_2(BH_4)_5$]/LiCl) obtained after first extraction (1st EXT) at 42°C.

Fig. 11. Isothermal volumetric desorption curves at 100°C under 1 bar H_2 pressure for a) 1h synthesized (($Mn(BH_4)_2$)/LiCl)+5 wt.% graphene), b) ($Mn(BH_4)_2$)/LiCl)+5 wt.% Ni) and c) (($Mn(BH_4)_2$)/LiCl)+5 wt.% $LiNH_2$).

Fig. 12. a, b, c) An example of the Arrhenius plots of rate constant k with temperature (100, 150 and 200°C) for estimation of the apparent activation energy of hydrogen desorption for three samples of 1h synthesized ($Mn(BH_4)_2$)/LiCl)+5 wt.% $LiNH_2$). d) A bar graph of the apparent activation energy (kJ/mol) for dehydrogenation for the 1h synthesized samples with and without additives with the corresponding error bars. The $LiNH_2$ additive exhibits the lowest apparent activation energy.

Fig. 13. Volumetric desorption curves at 100°C for a) ([{$Li(Et_2O)_2$}$Mn_2(BH_4)_5$]/LiCl) obtained after first extraction (1st EXT) at 42°C and b) ([{$Li(Et_2O)_2$}$Mn_2(BH_4)_5$]/LiCl) obtained after second extraction (2nd EXT) at 42°C. Volumetric desorption curves at 200°C for c) ([{$Li(Et_2O)_2$}$Mn_2(BH_4)_5$]/LiCl) obtained after first extraction (1st EXT) at 42°C and d) ([{$Li(Et_2O)_2$}$Mn_2(BH_4)_5$]/LiCl) obtained after second extraction (2nd EXT) at 42°C.

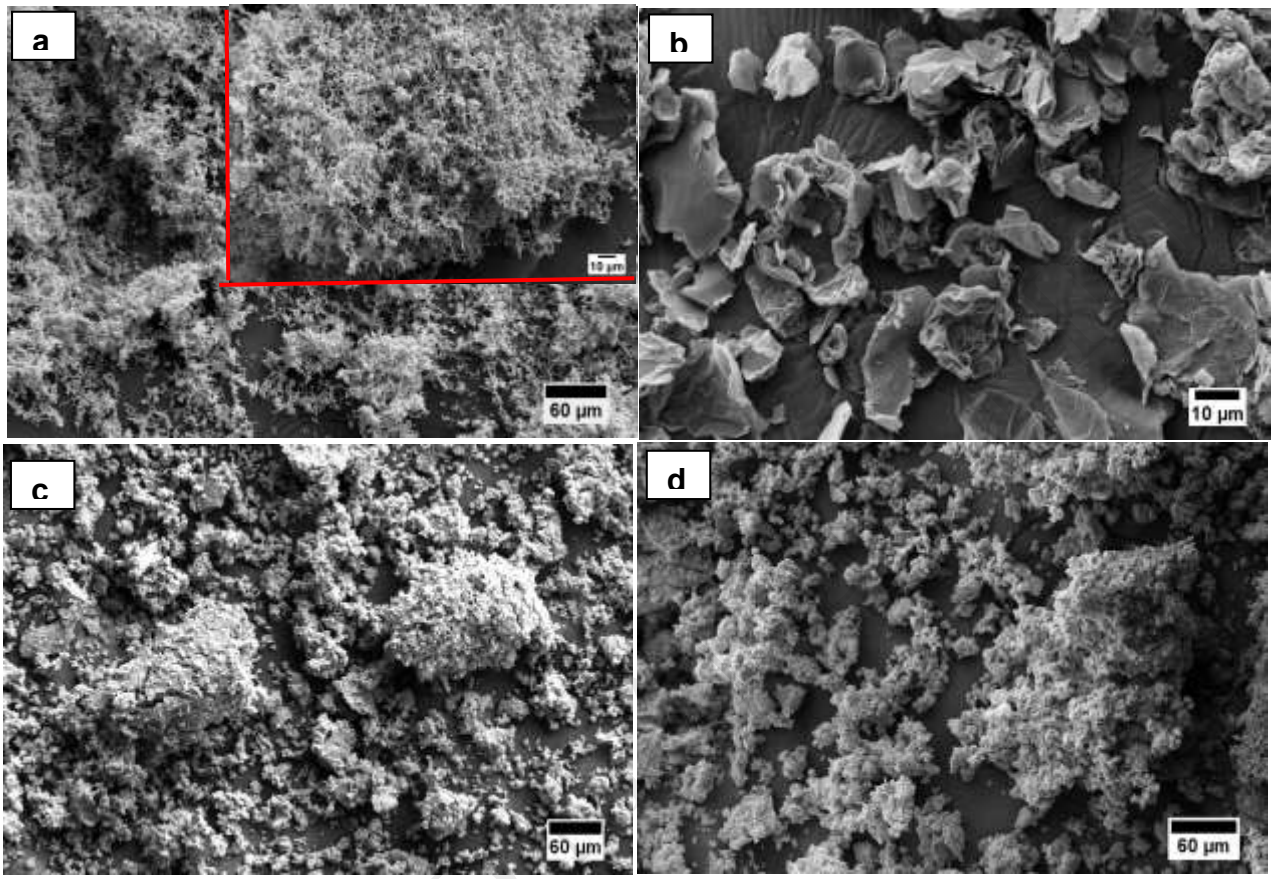

Fig. 1. Varin et al.

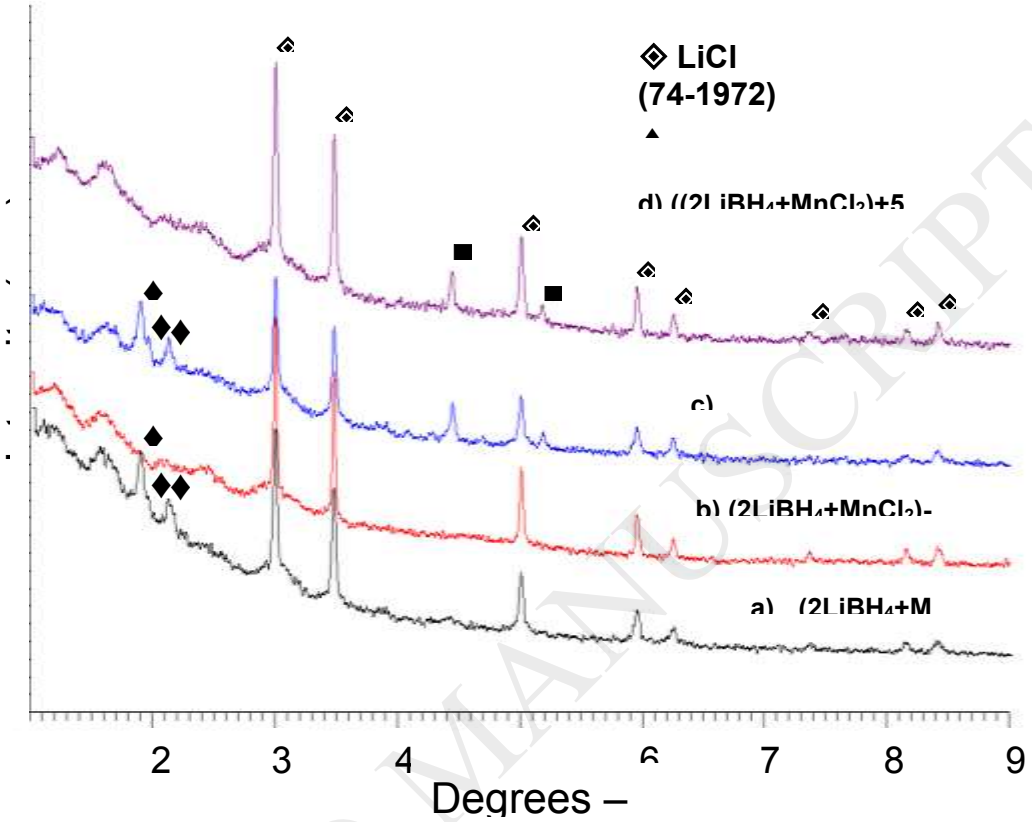

Fig. 2. Varin et al.

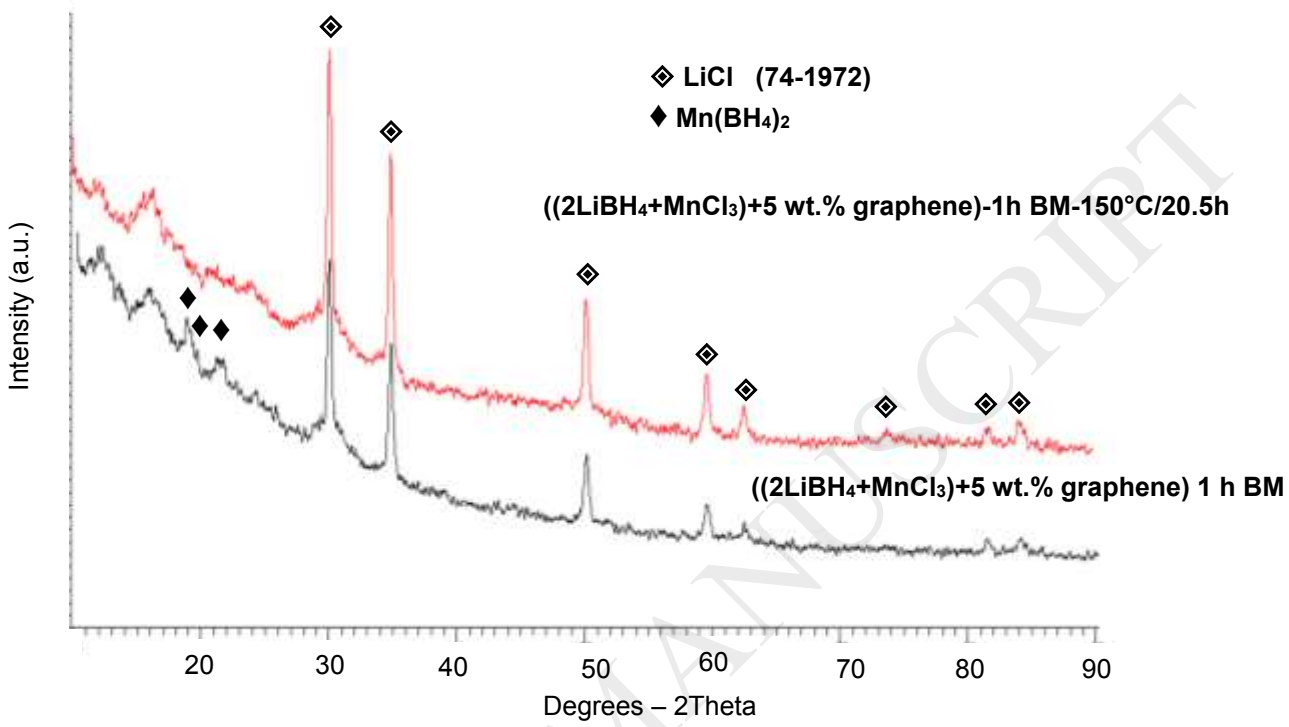

Fig. 3. Varin et al.

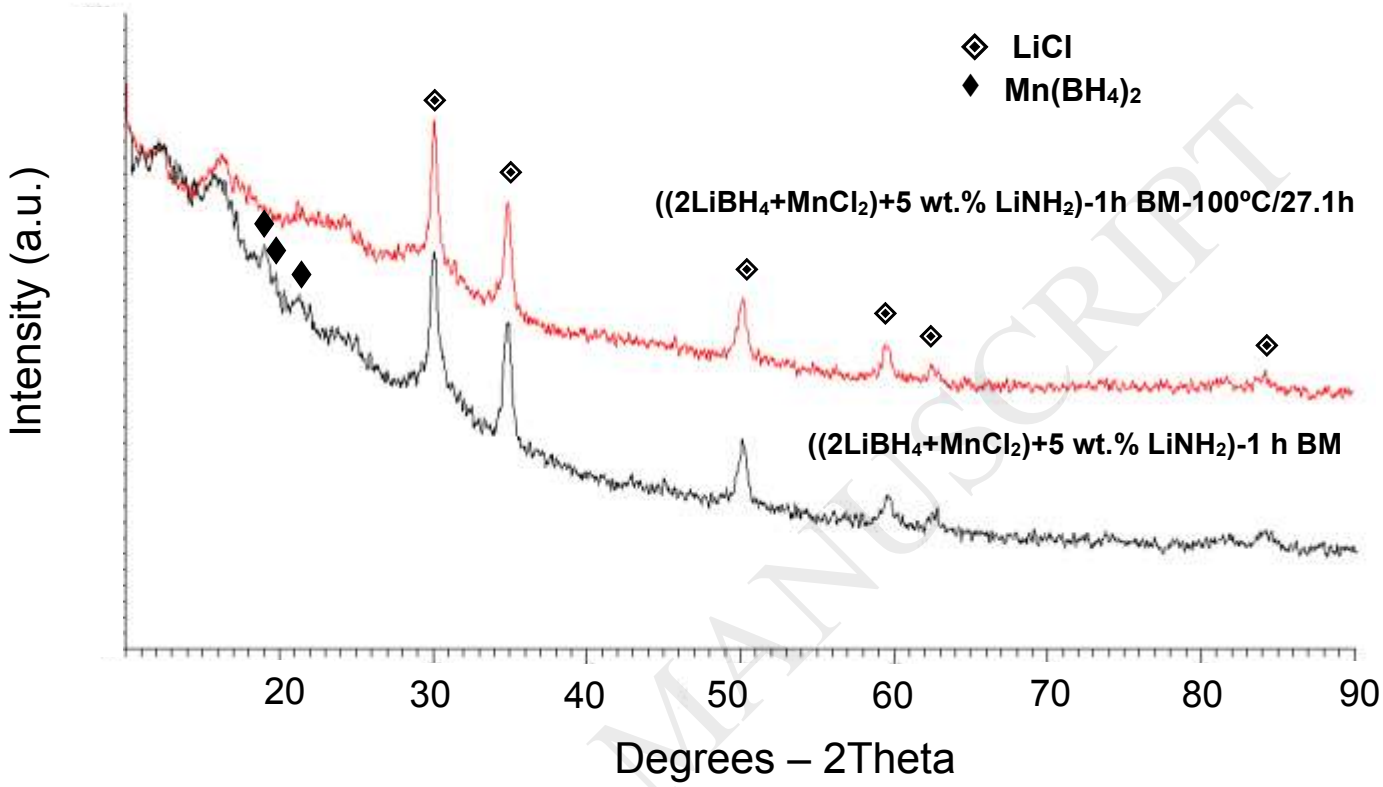

Fig. 4. Varin et al.

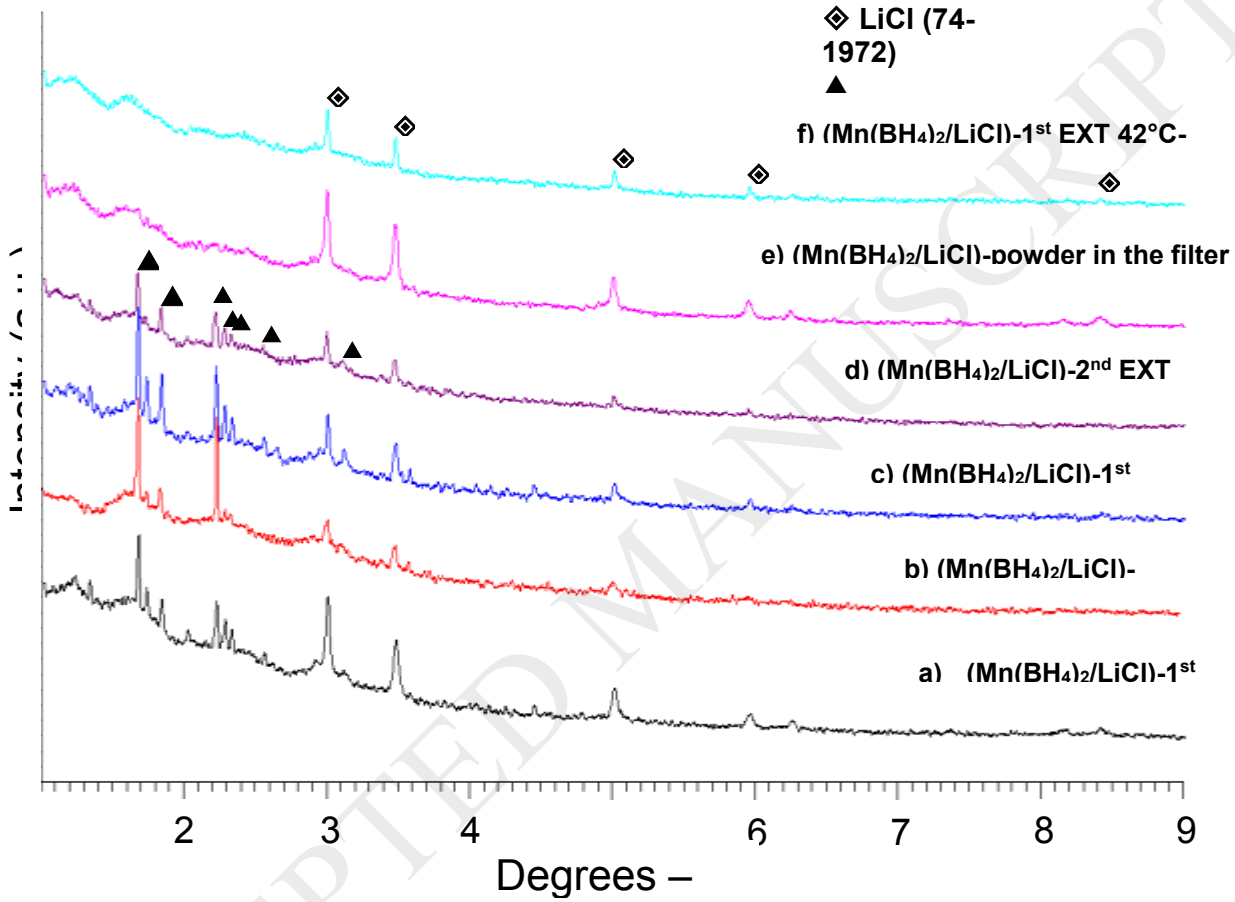

Fig. 5. Varin et al.

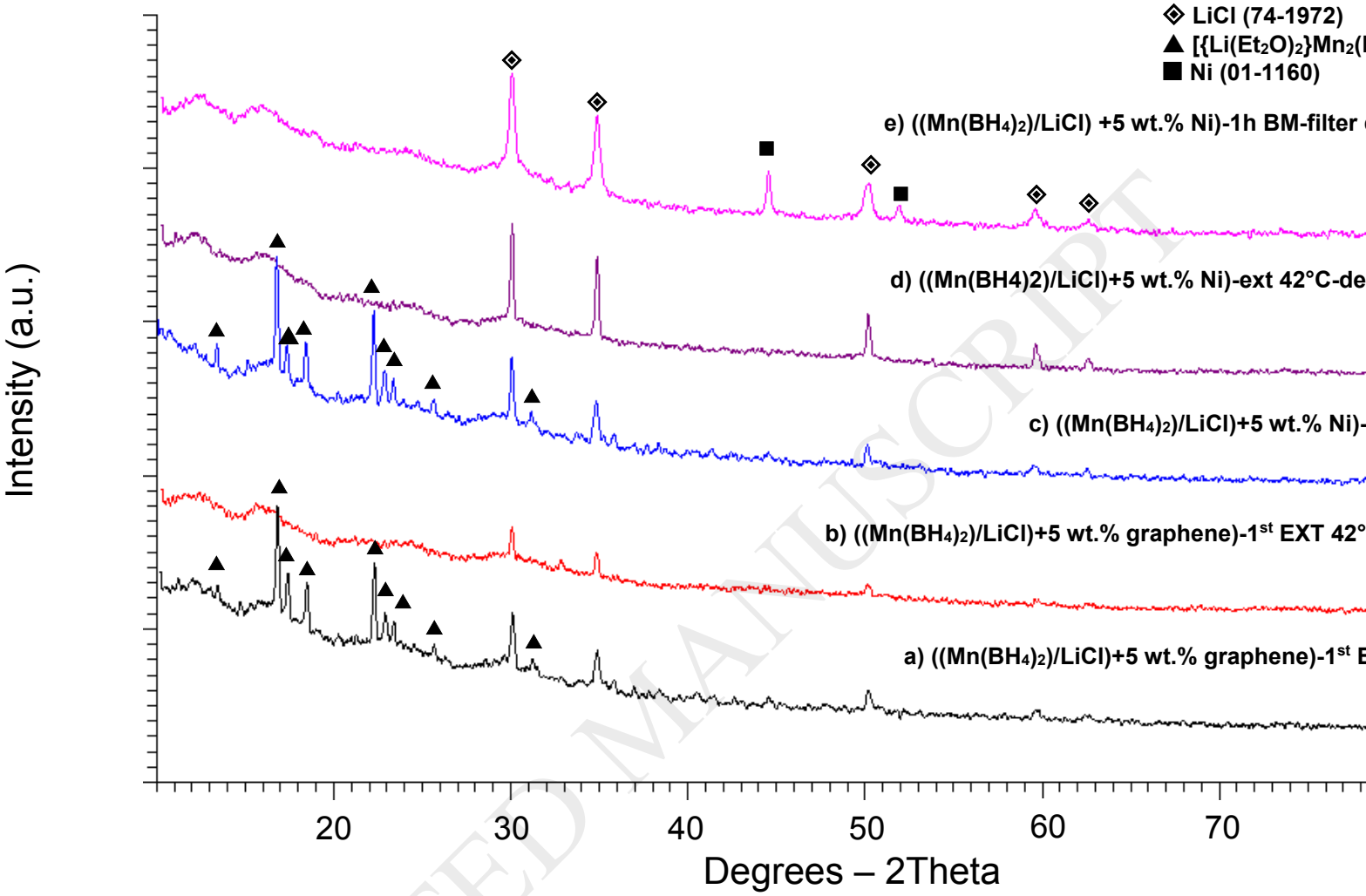

Fig. 6. Varin et al.

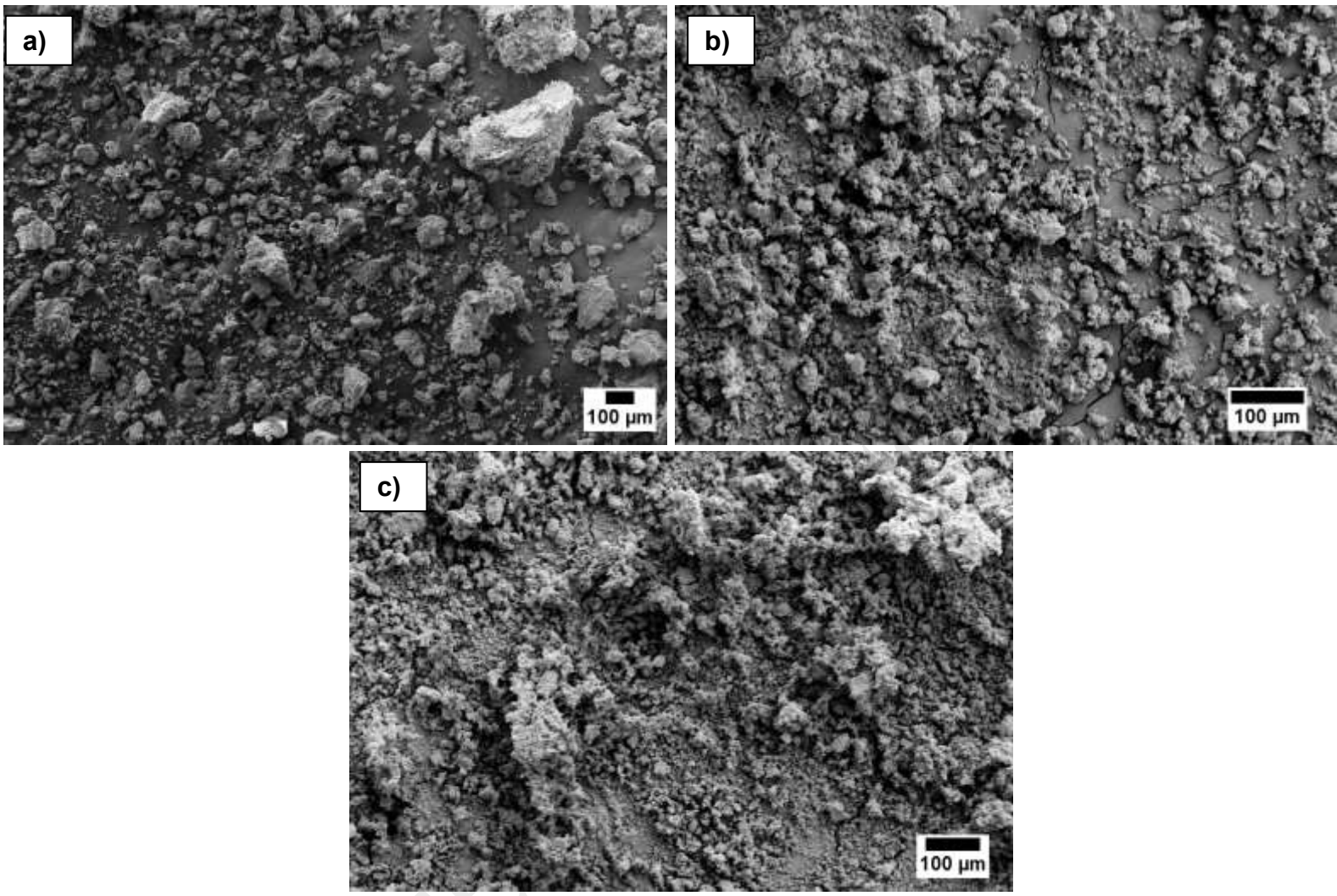

Fig. 7. Varin et al.

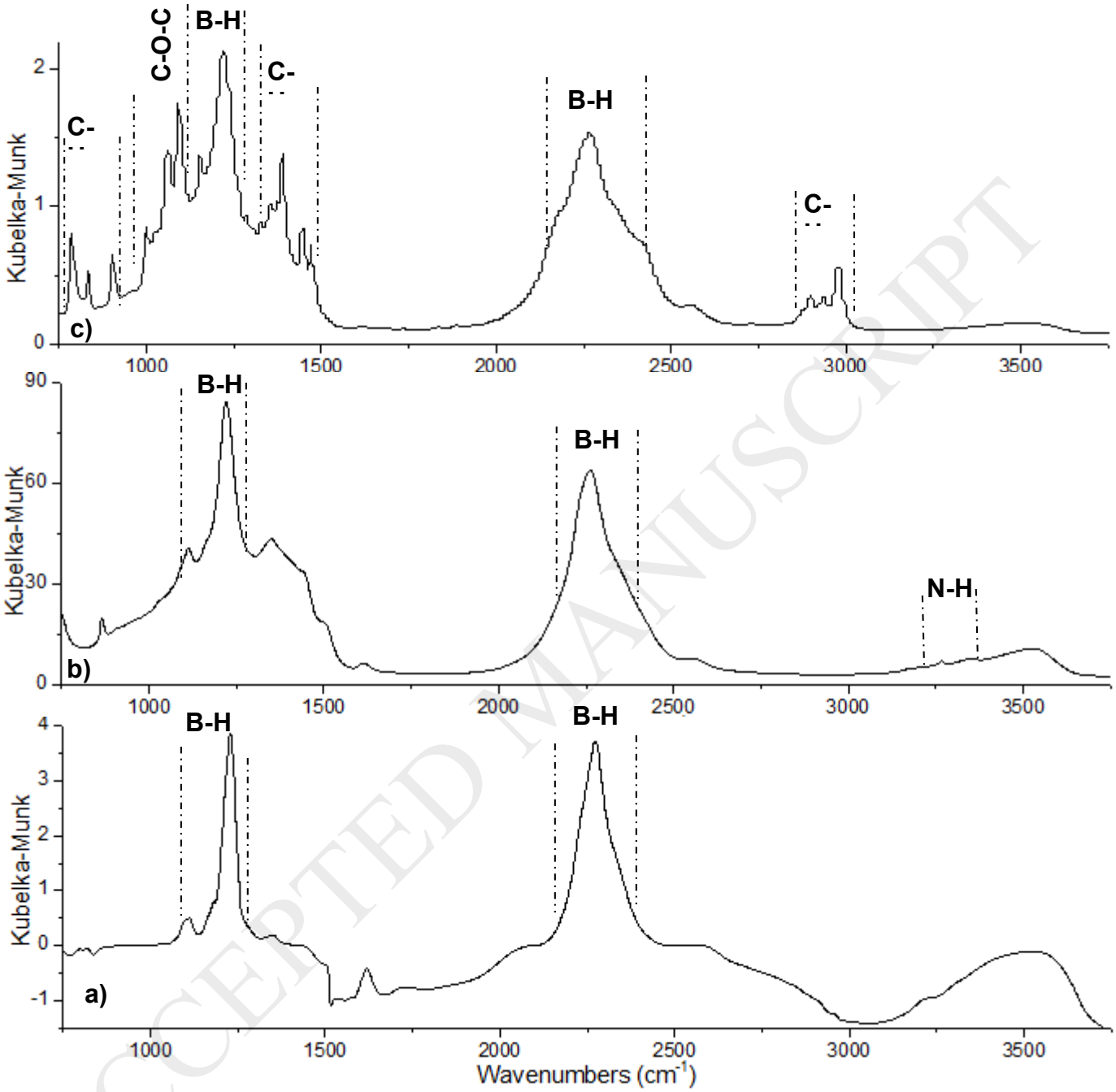

Fig. 8. Varin et al.

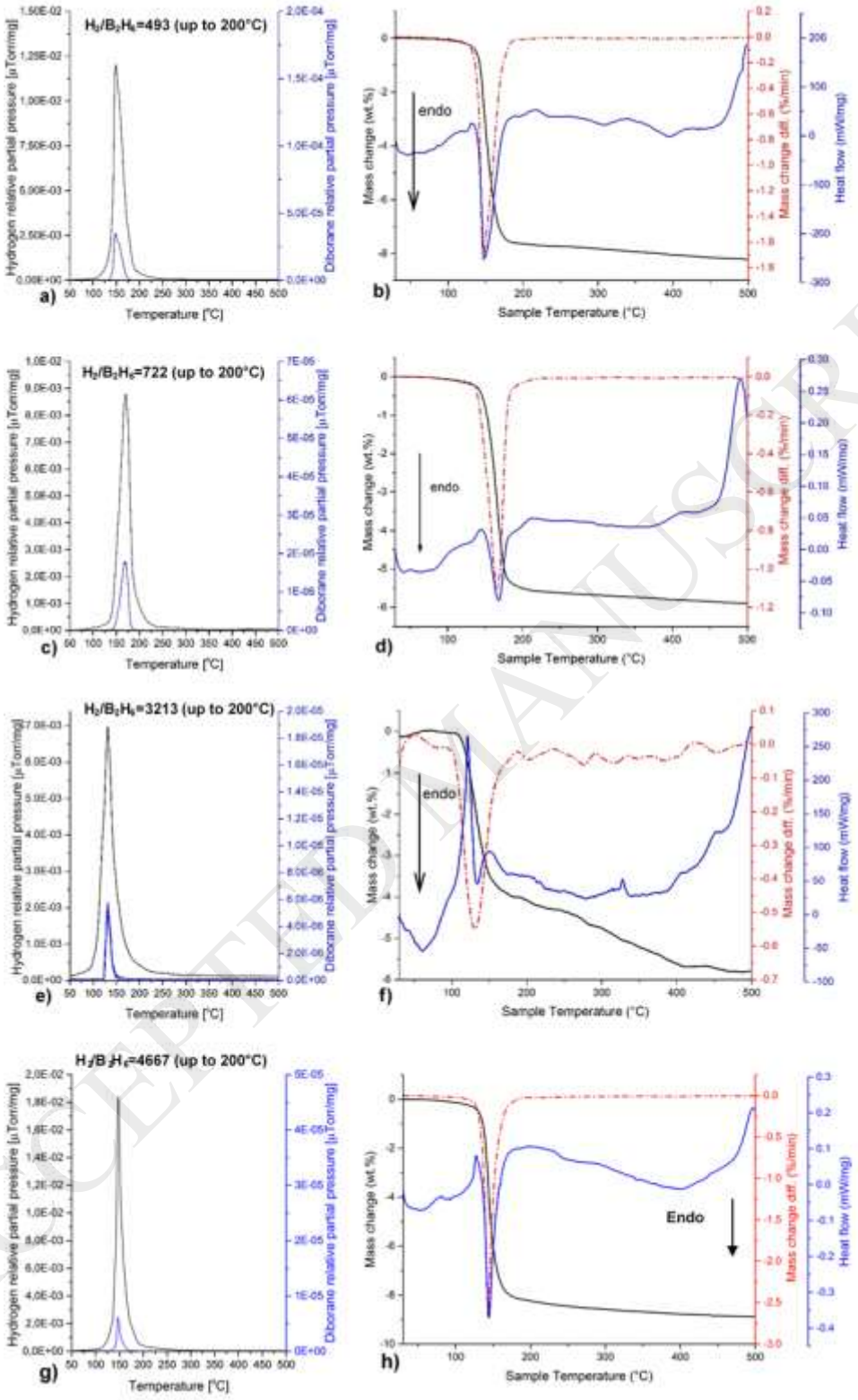

Fig. 9. Varin et al.

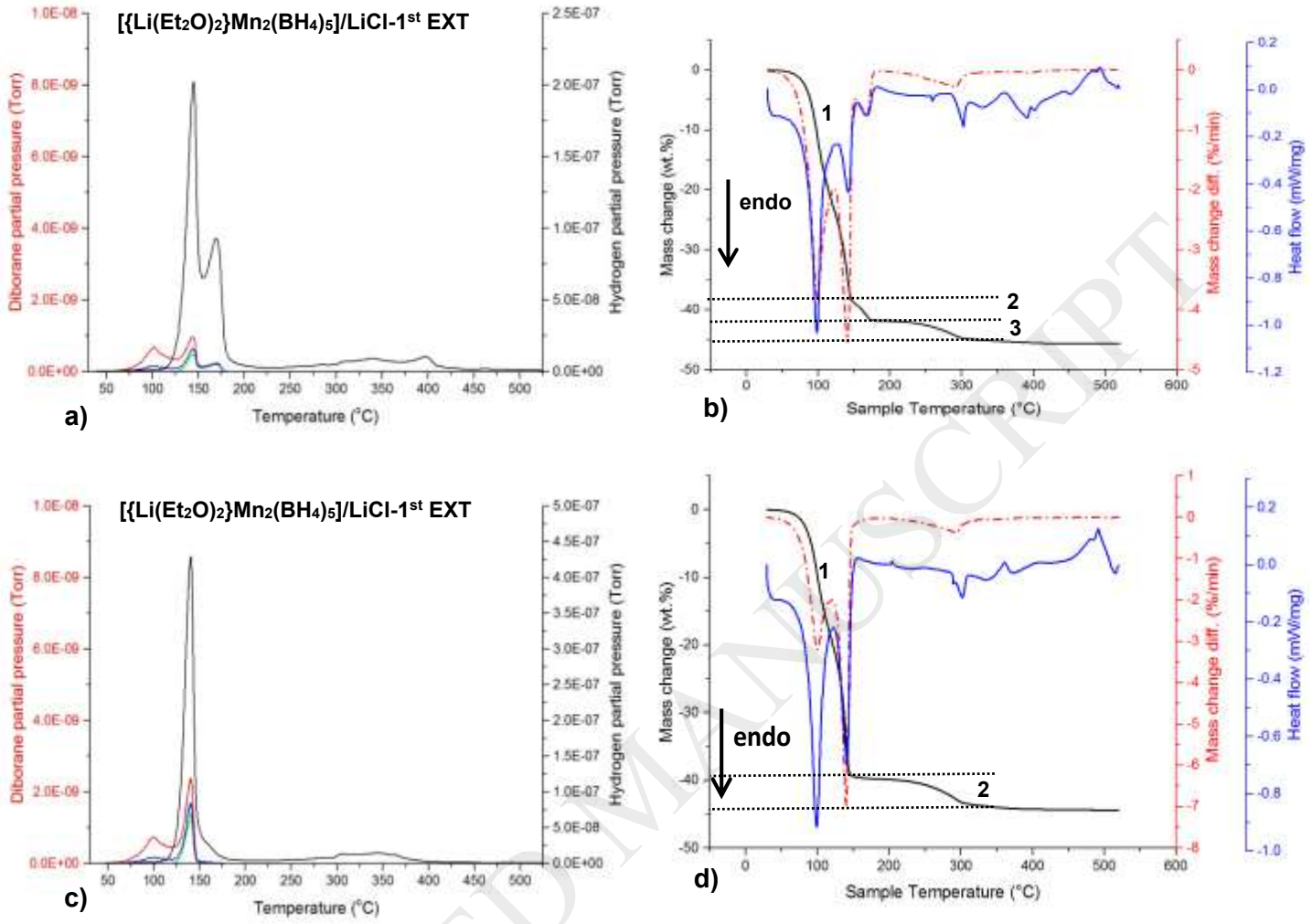

Fig. 10. Varin et al.

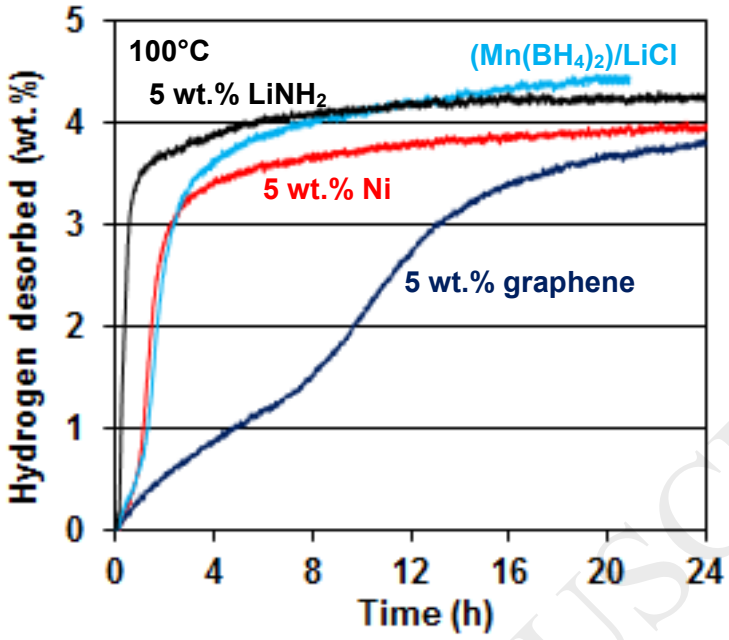

Fig. 11. Varin et al.

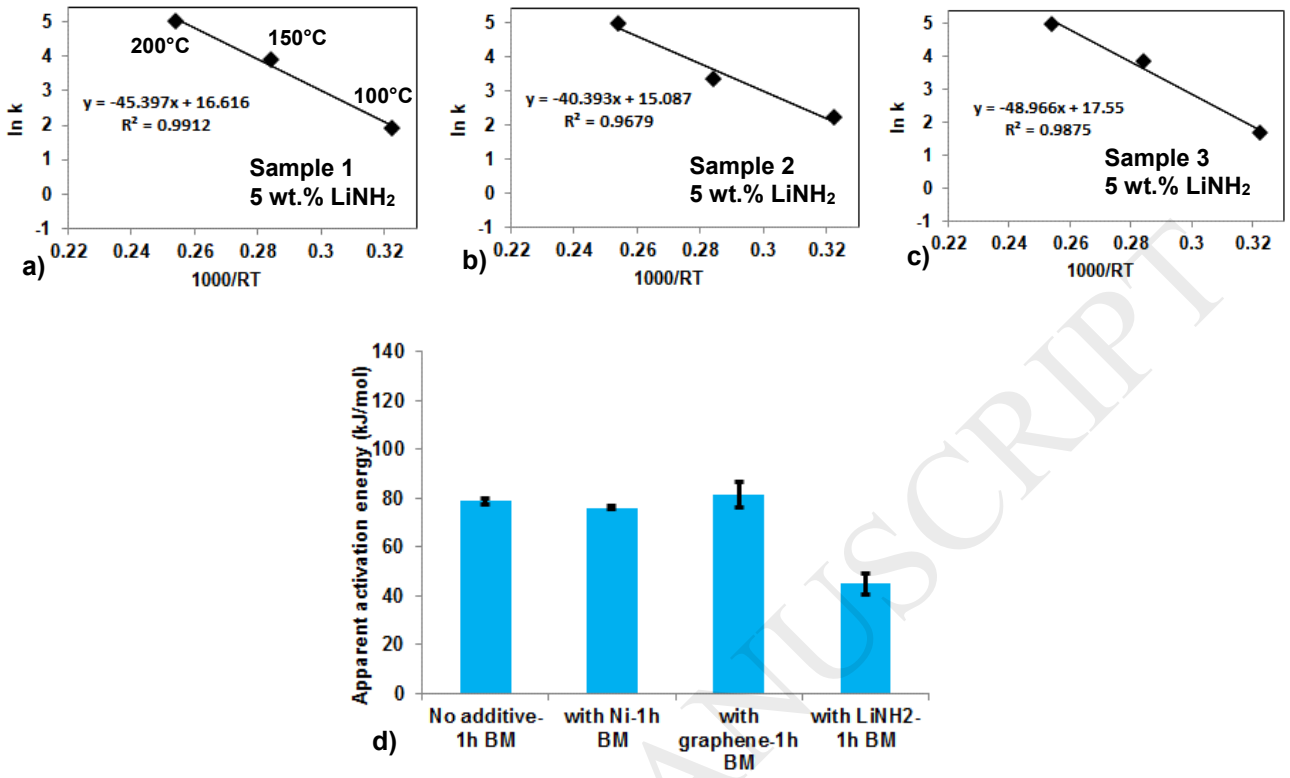

Fig. 12. Varin et al.

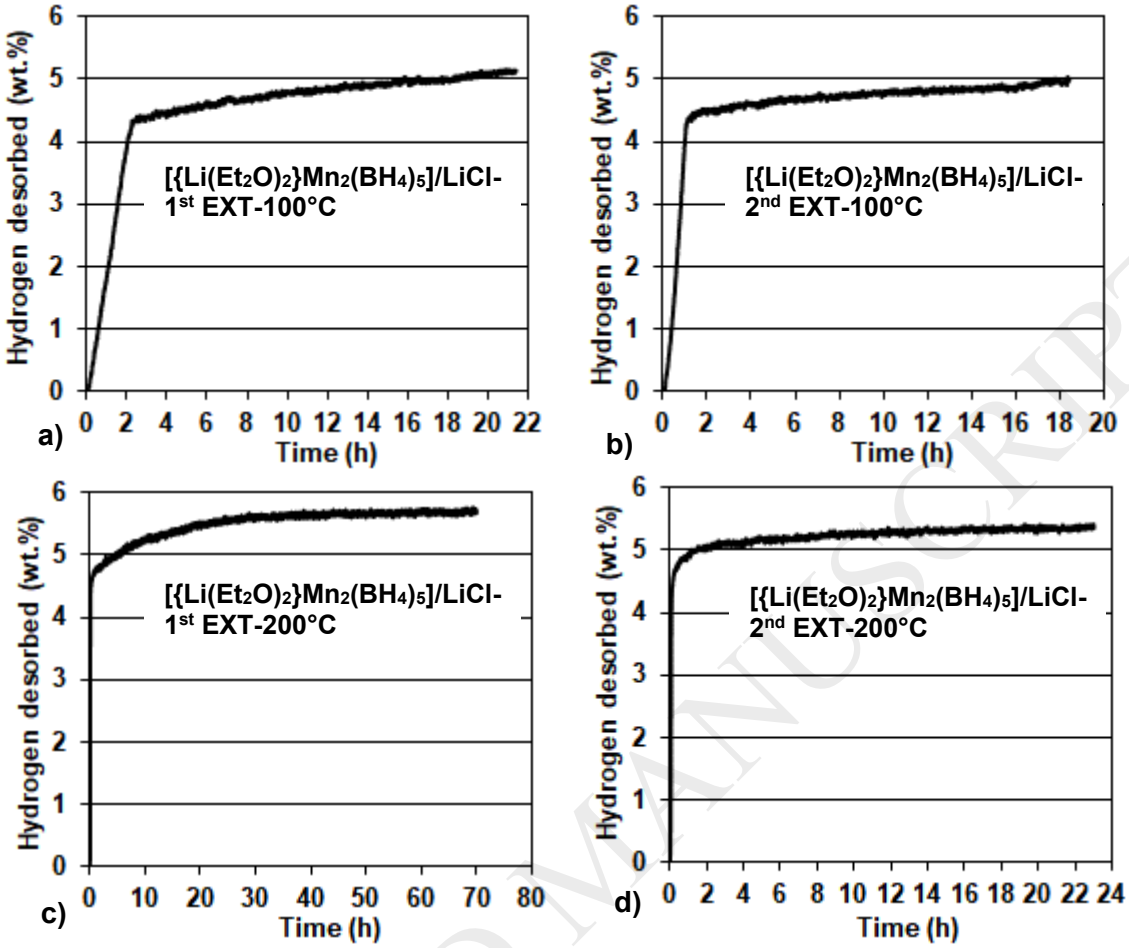

Fig. 13. Varin et al.